Chemical Geology 658 (2024) 122119



Contents lists available at ScienceDirect

Chemical Geology

journal homepage: www.elsevier.com/locate/chemgeo

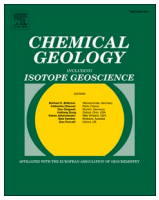



Unravelling the effects of magmatic fractionation, fluid phase separation and dilution on the composition of magmatic-hydrothermal fluids of the Cornubian Batholith (SW England)

Mauro Bongiovanni [a,*], Tobias Fusswinkel [a], Michael A.W. Marks [b]

[a] Institute of Applied Mineralogy and Economic Geology, RWTH Aachen University, Wüllnerstrasse 2, D-52062 Aachen, Germany
[b] Department of Geosciences, Eberhard-Karls-Universität Tübingen, Schnarrenbergstrasse 94-96, D-72076 Tübingen, Germany

ARTICLE INFO

Editor: Marco Fiorentini

Keywords:
Fluid inclusions
Geochemistry
Cornubian batholith
In situ LA-ICP-MS

ABSTRACT

The compositional evolution of magmatic-hydrothermal fluids from the Sn—W mineralized Cornubian batholith was investigated via in situ fluid inclusion LA-ICP-MS microanalysis and reveals a large degree of variation between intrusive stages and at the sample scale, with complexities due to superposition of several mechanisms affecting fluids chemistry during the protracted evolution of the batholith. Despite large ranges of salinities (from <1 wt% to 48 wt% $NaCl_{eq.}$), the effects of individual processes such as magmatic differentiation, fluid saturation and boiling, fluid mixing and dilution can all be discerned on the basis of fluid inclusion trace element geochemistry combined with detailed petrography and microthermometry.

In all samples, different fluid types (aqueous liquid-rich, vapor-rich and brine inclusions) were identified in variable proportions and microthermometry revealed complex temporal trends. Granite-related samples from the G5 intrusive stage are characterized by intermediate density fluids undergoing magmatic fractionation under pressure conditions above 1.5 kbar, indicated by successively decreasing fluid salinities with concomitant increases in Li, B, Rb and Cs concentrations. The latter two elements later strongly partitioned in the brine phase upon boiling, together with most of the other Cl-complexing elements (e.g., Fe, Mn, Pb, Zn). Those brines subsequently underwent progressive dilution with meteoric waters that caused a decrease in the concentration of all elements (besides B) and homogenization temperatures. In G3 granite from Dartmoor, on the other hand, brine inclusions represent the earliest fluid type while intermediate density fluids are absent, and a large salinity range in the fluid inclusion record associated with a decrease in homogenization temperatures represents their progressive dilution with meteoric fluid. The lack of intermediate density fluids at Dartmoor indicates fluid exsolution at relatively low pressures resulting in immediate phase separation into brine and vapor.

All studied samples associated with ore mineralization display only the trend of dilution of high-salinity magmatic fluids. Their transition metal contents (e.g. Fe, Mn, Pb and Zn) show the expected positive correlation with salinity of the fluids. Conversely, the compositional trends observed for Sn and particularly W are more enigmatic, as they do not appear to significantly fractionate during most of the physicochemical processes outlined above and appear to be unrelated to fluid salinity, opposite of what would be expected for Sn as it is dominantly transported in Cl-complexes.

This study highlights the key advantages of high-resolution geochemical fluid inclusion studies in discerning a variety of magmatic and post-magmatic processes in fluids in comparison to bulk fluid inclusion techniques or more simplistic fluid inclusions studies which might overlook important aspects of the typically complex history of fluids evolution in magmatic-hydrothermal systems.

* Corresponding author.
E-mail address: mauro.bongiovanni@emr.rwth-aachen.de (M. Bongiovanni).

https://doi.org/10.1016/j.chemgeo.2024.122119
Received 1 September 2023; Received in revised form 24 April 2024; Accepted 26 April 2024
Available online 28 April 2024
0009-2541/© 2024 The Authors. Published by Elsevier B.V. This is an open access article under the CC BY license (http://creativecommons.org/licenses/by/4.0/).

1. Introduction

Many aspects of the genesis of magmatic-hydrothermal Sn and especially W ores are still controversial, particularly with regard to processes related to deposit formation from early to late stages of magmatic-hydrothermal activity (Heinrich, 1990; Audétat et al., 2008; Lecumberri-Sanchez et al., 2017; Korges et al., 2018; Lehmann, 2020). Tin-tungsten systems are typically associated with granitic intrusions and the Cornubian batholith (SW England) represents one of the best-studied examples of this type of ore system in Europe (Dines, 1956; Jackson et al., 1989; Alderton, 1993). These Sn—W systems can form a range of mineralization styles, such as lodes, veins with greisenized borders, stockworks and replacement bodies (Hosking, 1969). South-West England has been one of the biggest Sn—W (and kaolinite) mining districts of the world for over two centuries, and a critical location for the development of mining technologies (Gamble et al., 2020).

Despite the clear association of Sn—W deposits with granitic intrusions, the origin of the fluids responsible for the mineralization in the Cornubian batholith, and in general for these types of deposits, has been debated for decades. Many case studies emphasized the critical role of mixing between magmatic and possibly more oxidized meteoric water for the mineralization (Simpson et al., 1979; Jackson et al., 1989; Heinrich, 1990; Polya et al., 2000; Harlaux et al., 2021), while other studies considered direct precipitation from magmatic fluids involving either wall-rock interaction or interaction with other types of external fluids, such as metamorphic and basinal fluids (Jackson et al., 1982; Primmer, 1985; Wilkinson, 1990; London and Manning, 1995; Williamson et al., 2000; LeBoutillier, 2002; Lecumberri-Sanchez et al., 2017; Korges et al., 2018; Torró et al., 2024). Still, compositional fluid geochemistry data throughout the protracted lifetime of granitic systems related to Sn—W deposits remain scarce, but may be key in furthering our understanding of deposit formation.

Fluid inclusions trapped in minerals related to mineralization represent key evidence in resolving the nature of ore-forming fluids and the processes of ore formation. The trace element geochemistry of Cornubian Sn—W ore fluids has been studied by means of bulk analytical techniques (Bottrell and Yardley, 1988; Alderton et al., 1992; Smith et al., 1996; Gleeson et al., 2001), which yield an average geochemical characterization of all inclusions present in the sample but cannot be applied to samples recording multiple fluid pulses (Wagner et al., 2016). Mass balance dictates that the values obtained with bulk-analytical techniques of such complex samples are biased by the inclusions containing the highest salinities, and therefore the highest concentrations of most elements (e.g. Chi and Savard, 1997). Conversely, LA-ICP-MS fluid inclusion microanalysis provides a spatial resolution that allows to analyze individual fluid inclusions in situ, enabling the study of complex samples recording sample-scale mixing processes or containing a multitude of fluid types (Fusswinkel et al., 2013; Wagner et al., 2016).

This study presents and discusses the results from the first comprehensive LA-ICP-MS fluid inclusions study of the magmatic-hydrothermal system of the Cornubian batholith.

2. Geological setting

The Cornubian batholith formed in a post-collisional environment following the Variscan orogeny in the early Permian, and is hosted in a series of passive margin sedimentary basins formed in Devonian and Carboniferous with a very low grade metamorphic overprint (Warr et al., 1991; Shail and Leveridge, 2009). Its dimensions, including the offshore extension, are estimated to be around 250 by 20–40 km, with a thickness of several km (Willis-Richards and Jackson, 1989; Taylor, 2007), exposed as six main plutons and several minor stocks of granite, that likely rose through dykes and emplaced as shallow laccoliths (Pownall et al., 2012; Drivenes et al., 2016). The batholith formed over a

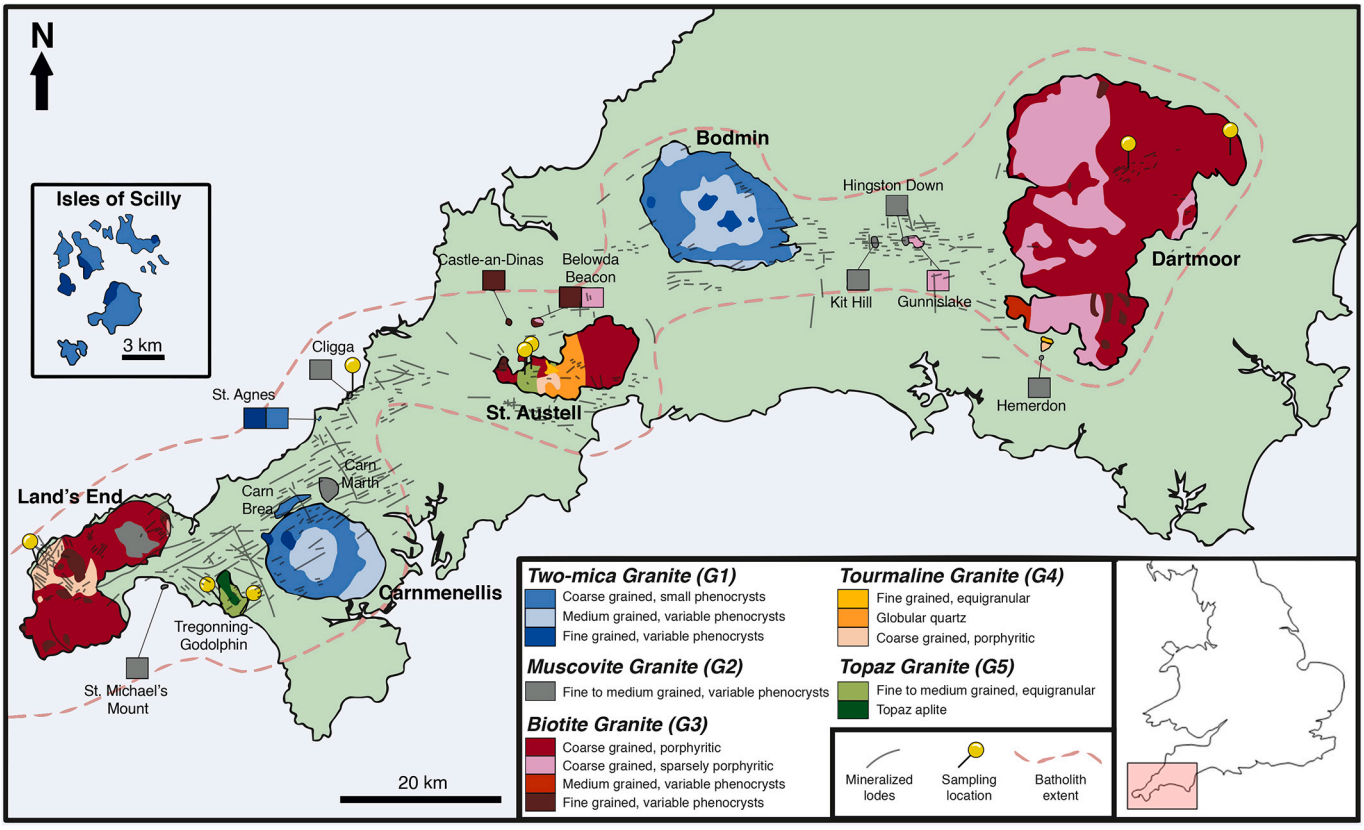

Fig. 1. Schematic geological map of the Cornubian batholith showing the distribution of the main igneous bodies according to the classification by Simons et al. (2016) and of the mineralization (locality names not labelled). Modified after Hughes (2018) and Gleeson et al. (2000).

span of at least 20 Ma, starting at ca. 293 Ma, with the main Sn-W-Cu mineralization occurring in the latest part of this period (Chen et al., 1993; Chesley et al., 1993; Clark et al., 1993). Given its textural and mineralogical heterogeneity, several classifications of the granites have been suggested (e.g. Exley and Stone, 1964; Dangerfield and Hawkes, 1981; Cobbing and Clarke, 2006). The currently most widely used classification (Simons et al., 2016; Fig. 1) discriminates five types of granite, with G1-G2 (two-mica and muscovite granite, respectively) representing the first fractionation series, followed by G3-G4 (biotite and tourmaline granite) representing a second phase, with a slight variation in the conditions of partial melting (higher temperature and lower pressure), and finally G5 (topaz granite) whose origin is still debated (Manning and Hill, 1990; Stone, 1992; Simons et al., 2016). Granitic and rhyolitic dykes are widespread across the batholith. All granites possess a typical peraluminous and S-type granite signature (Chappell and Hine, 2006). The proportion of the micas and tourmaline can vary significantly and in younger granites tourmaline becomes prevalent and muscovite is rare (Simons et al., 2016). Texturally, the granites are variable across the region, with diverse porphyricity and grain sizes, despite chemical similarities (Manning et al., 1996; Cobbing and Clarke, 2006; Simons et al., 2016).

The Sn—W mineralization occurs mainly in greisen-bordered sheeted vein complexes, of which Cligga Head and St. Michael's Mount represent well-known examples, as well as lodes, such as those at South Crofty and Geevor (Scrivenor, 1903; Dines, 1956; Hall, 1971; Moore and Jackson, 1977; Mount, 1985; Campbell and Panter, 1990). Overall, W-rich veins usually pre-date cassiterite deposition, with Hemerdon being one of the largest W deposits in the world (Tapster et al., 2017; Wilkins et al., 2017; Idoine et al., 2023). Cassiterite sometimes occurs not only within the veins, but also in the greisenized halo (Wilkins et al., 2017).

In the Cornubian region, Sn mineralization also occurs in association with Cu and other base metals polymetallic veins, mainly in the form of multi-stage lodes, and subordinate stockworks and replacement deposits (Scrivener, 2006). Individual lodes exhibit a pronounced zoning with proximity to the intrusive centers (called "telescoping" by Hosking, 1969), with typically endogranitic Sn-rich domains surrounded by Cu-bearing veins in the proximal area around the contact with the host rock and finally by distal Pb—Zn mineralization, which are mainly hosted in the country rocks (Dines, 1956; Hosking, 1964).

The origin of the Sn—W greisens and the Sn-Cu-As polymetallic ore deposits has been discussed over the years, but most authors agree on a predominantly magmatic component in the fluids (Dines, 1956; Jackson et al., 1989; Wilkins et al., 2017). Jackson et al. (1989) attributed the telescoping feature of the polymetallic veins to a successively increasing meteoric water component to the magmatic-hydrothermal ore fluids. Distal to the intrusive centers, hydrothermal veins locally known as "crosscourses" carry base metal mineralization as well, but are considered to be Triassic in age and unrelated to magmatic activity, based on their low-temperature mineral assemblages, fluid geochemistry (influenced by mixing with basinal $CaCl_2$-rich brines) and their structurally distinct occurrence in N-S trending veins, while the polymetallic Sn-Cu-As lodes occur in predominantly E-W orientations (Dines, 1956; Scrivener et al., 1994; Gleeson et al., 2000; Scrivener, 2006).

The various granite types are exposed as distinct plutonic bodies throughout Cornwall and Devon (Fig. 1). The Dartmoor pluton is mainly composed of G3 granite and is characterized by scarce Sn—W mineralization in comparison with the rest of the Cornubian batholith (Dines, 1956). An exception is represented by the area around Birch Tor, which has been one the biggest mining districts of SW England and where tourmaline-quartz-cassiterite veins and cross-cutting quartz-hematite veins occur (Dines, 1956; Scrivener, 1982). Several Sn-bearing alluvial deposits were found and exploited around Dartmoor, although their source is still unclear (Dines, 1956; Scrivener, 1982).

The composite Land's End pluton is formed by at least three discrete plutonic bodies (classified as G2, G3 and G4 granites) that have a significant variability in texture (Simons et al., 2016; Hughes, 2018). It hosted several mining districts, in particular in areas exposing G4 granite: here most of the mineralization occurs in lodes (typically rich in Sn and Cu) near the contacts towards the metasedimentary country rock. Replacement deposits containing economic grades of Sn mineralization, such as skarns and "tin floors" occur in the areas of Levant and Botallack, and are characterized by highly variable parageneses and strong degrees of granite alteration (Dines, 1956; Hosking, 1969; Dominy et al., 1996; Hughes, 2018).

The St. Austell pluton exposes three distinct granite types (G3, G4 and G5 granites; Manning and Exley, 1984; Simons et al., 2016), partly showing strong kaolinization. This district has been mined for decades for kaolinite and several open-pit mines expose the granites (Bristow and Exley, 1994). In some areas, tourmaline-rich breccias (e.g., Wheal Remfry) are found, while Sn—W mineralization across the pluton is relatively scattered and typically consists of vein complexes with variable mineral assemblages. The St. Austell pluton and the Tregonning-Godolphin stock host most of the G5 topaz granite exposures in the Cornubian batholith, with topaz reaching modal abundances of 25–30% (Collins and Coon, 1914; Williamson et al., 1997).

Unidirectional solidification textures (UST) are widespread across the entire Cornubian batholith and provide field evidence of cyclic events of magmatic fluid saturation, unmixing and release via overpressure along the crystallization fronts of the granite. They can be observed at Porthmeor Cove, Megiliggar Rocks, St. Micheal's Mount, and in several occurrences in the St. Austell pluton, typically at the contact between different granite facies or types (Jackson and Power, 1995; LeBoutillier, 2002; Müller et al., 2006). In the first two locations mentioned above, a layering of alternating pegmatites and aplite is observed.

The other three main plutons, Bodmin, Carnmenellis and Isles of Scilly, are formed entirely by G1 and G2 granites (Fig. 1). Fractionation from G1 to G2 strongly enriched Sn and W and greisen-bordered sheeted vein complexes are spatially associated with G2, especially in smaller stocks such as Cligga, Hemerdon and St. Michael's Mount (Exley and Stone, 1964; Moore and Jackson, 1977; Dominy et al., 1995; Jackson and Power, 1995; Simons et al., 2017).

3. Material and methods

3.1. Samples selection

Given the regional scale purpose of this study, representative samples were taken from the various granite types and mineralization styles to serve as a proxy for similar occurrences throughout the district. The aim was to have a full representation of magmatic and hydrothermal material occurring at various locations across the Cornubian batholith, assuming it evolved as discrete systems, taking into account spatial and temporal differences. This includes granites of different types, miaroles and pegmatites, and hydrothermal veins of various morphology and mineralization paragenesis. Care was taken to sample only the least weathered material available, and all sections were prepared from fresh surfaces near the cores of the specimens.

70 samples from 16 different localities were collected during fieldwork. In addition, previously collected samples described in Duchoslav et al. (2017) were used from the archive of the University of Tübingen. A first selection was done macroscopically, on the basis of alteration, quartz abundance and aspect, and relevance in the overall picture of the magmatic-hydrothermal system. For the samples from Duchoslav et al. (2017), available thin sections were used as additional material to evaluate the quality of the samples for the present study prior to preparation of new sections. Ultimately, nine samples, spanning the entire evolution from magmatic to hydrothermal at selected sites of the Cornubian batholith, were selected for further analyses. In particular, two granites (G3 and G5) were selected as representative of intermediate and late differentiated magmas; a pegmatite and a miarolitic cavity hosted in G5 and a barren quartz vein cutting through the G5 granite were picked

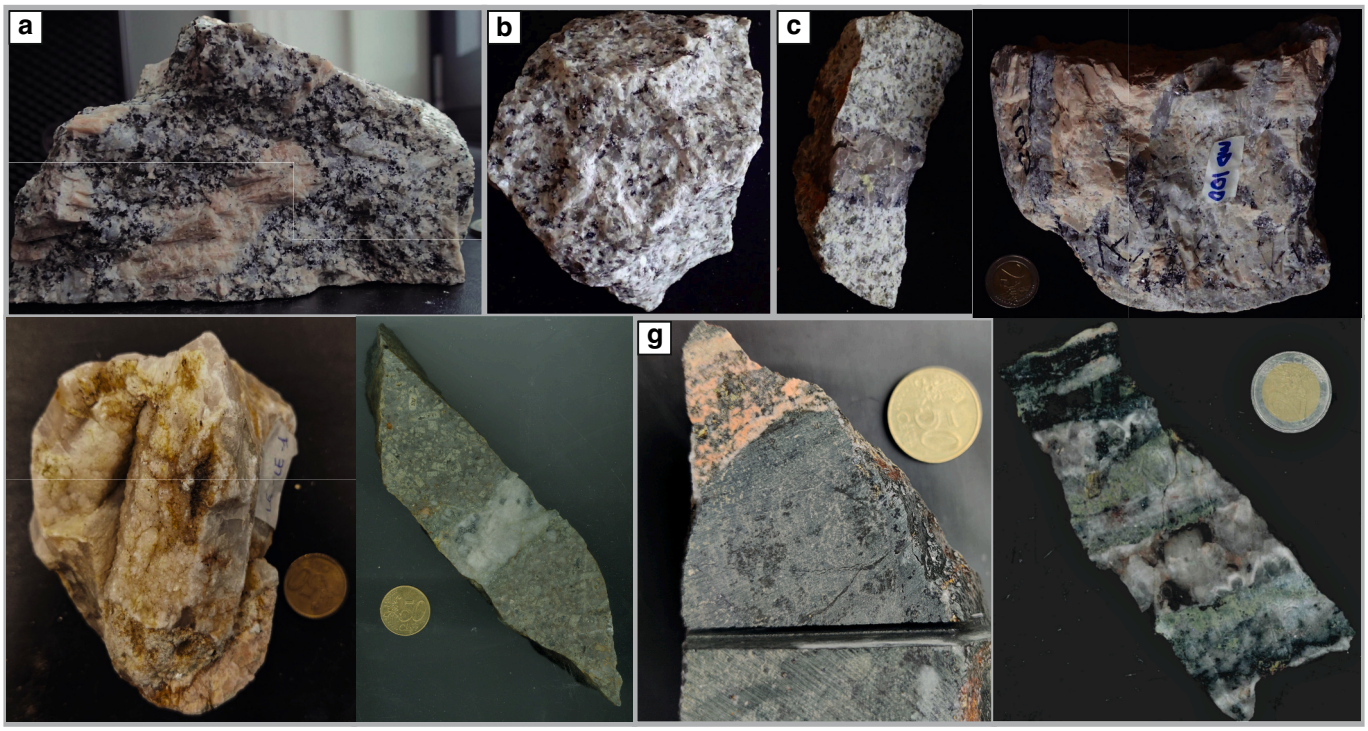

Fig. 2. Macroscopic photographs of the samples from this study. a) Porphyritic biotite granite (21MD1); b) Equigranular topaz granite (21MD219); c) Quartz-vein in topaz granite (21MD222); d) Layered pegmatite-aplite with combed K-feldspars (21MD100I); e) Euhedral quartz on mica and feldspar from a miarolitic cavity (LELE); f) Greisen-bordered quartz-arsenopyrite vein (SCH1); g) Fluorite-chalcopyrite-arsenopyrite vein at the contact granite-greenstone, with zoomed view on the bottom left (21MD65); h) Multi-infill endogranitic veins, with an early episode with quartz-tourmaline(−cassiterite) fill and tourmalinized borders, and a later specular hematite-quartz veining. Two sections were prepared from this sample, representing two different subparallel veins (21MD10S and 21MD10B).

Table 1
Summary of the provenance and paragenesis of the selected samples. In the penultimate column the fluid inclusions host minerals are specified. To reference the later geochemical data figures, sample summary names are listed. Abbreviations: Qtz - quartz; Fl - fluorite; Apy - arsenopyrite; Cpy - chalcopyrite.

Sample	Locality	(Host) granite	Description	F.I. host	Summary name
21MD1	Blackingstone	G3 (Dartmoor)	Biotite-rich granite with K-feldspar phenocrysts	Quartz	G3 granite
21MD219	Treviscoe	G5 (St. Austell)	Topaz-rich equigranular granite	Quartz Topaz	G5 granite
21MD222	Treviscoe	G5 (St. Austell)	Quartz vein in Topaz-rich equigranular granite	Quartz	Qtz vein in G5
21MD100I	Megiliggar Rocks	G5 stock	Pegmatite with UST K-feldspar, tourmaline, interstitial quartz and aplite layer	Quartz	G5 pegmatite
LELE	Lesceave Par	G5 stock	Miarolitic cavity with euhedral quartz growing on K-feldspars and white mica	Quartz	G5 miarolitic
SCH1	Cligga Head	G2 stock	Greisen-bordered quartz vein with sparse arsenopyrite clusters	Quartz	Greisen vein
21MD65	Botallack	G4 (Land's End)	Vein at the contact granite-greenstone, filled with fluorite, chlorite, arsenopyrite and chalcopyrite	Fluorite	Fl-Apy-Cpy vein
21MD10S	Birch Tor	G3 (Dartmoor)	Endogranitic quartz vein with specular hematite near a tourmalinized bordered veinlet	Quartz	Hem-Qtz-Tur vein
21MD10B	Birch Tor	G3 (Dartmoor)	Endogranitic vein with earlier quartz and chalcedony infill, and later quartz and hematite	Quartz	Hem-Qtz vein

to represent the magmatic-hydrothermal transition, and finally a greisen vein, a polymetallic vein and two veins of relatively low-temperature mineralized hydrothermal assemblages represent the hydrothermal stages. Sample details are presented in Fig. 2 and Table 1.

3.2. Fluid inclusion petrography

Doubly-polished ~400 μm thick sections were made for fluid inclusion petrography of the selected samples, and in some cases additional complementary 30 μm thin section were prepared for a classic petrographic description. The petrographic work was performed using a Leica DM4500P LED optical microscope in combination with a Leica DMC4500B camera.

The inclusions were described using the abbreviation L_nVX, where L and V indicate the liquid and vapor respectively, and n represent the proportion (in %) of the liquid phase. Finally, X indicates daughter crystals, if present (indicated as H if the solid phase is clearly identifiable as halite). Where possible, inclusions with dimensions above 20 μm were preferred, as they yield higher signal intensities during LA-ICP-MS analysis, which is strongly dependent on fluid inclusion volume. Selection was based on the fluid inclusion assemblage (FIA) concept (Goldstein and Reynolds, 1994). FIAs are defined as groups of coevally trapped inclusions in a petrographically constrained feature such as growth zones or healed fractures, containing only a single fluid type with consistent petrographic characteristics (phases and their volume proportions). Notable exceptions are FIAs recording fluid phase separation processes (boiling), which are characterized by the presence of both vapor- and liquid-dominated (or brine) inclusions in the same trail.

The relative chronology of FIAs within individual samples was carefully established on the basis of petrographic observation, and preference for the geochemical analyses was given to primary and pseudosecondary FIAs. However, for some samples only secondary trails were available and therefore selected, provided that their phase proportions and microthermometric behavior was internally consistent. Secondary fluid inclusions consisting of L_{100} (i.e., totally liquid, without vapor bubble) were excluded from the analysis as they formed at significantly lower temperature (and potentially pressure), or underwent significant post-entrapment modification.

3.3. Microthermometry

The microthermometric analysis was done with a Leica DM2700P microscope combined with a Linkam THMSG600 heating-freezing stage. The instrument was calibrated regularly using synthetic inclusions of the systems H_2O-NaCl-CO_2 (Q3 quadruple, −56.1 °C), H_2O-NaCl (eutectic, −21.2 °C) and pure H_2O (triple point and critical point, 0.0 °C and 371.2 °C).

Low-temperature microthermometric measurements were done first. Inclusions were rapidly frozen to temperatures around −80 °C (down to −130 °C for high salinity inclusions) and then heated at a rate of around 30°/min. When approaching the first observable melting of phases within the inclusion, the rate was slowed down to ~10°/min to determine the approximate temperature of formation of the first liquid. When approaching the final melting of one of the phases present, the rate was reduced to 1°/min and the temperature of the phase disappearance recorded. This allowed to obtain values with an accuracy of ±0.1 °C during replication experiments.

For FIAs containing a halite crystal at room temperature, high-temperature microthermometry was performed using the same instrument. The inclusions were first heated at high rates, and when approaching phase transitions the rates were reduced to ~5°/min, recording temperature values with an accuracy of ±1 °C. Homogenization temperatures represent the minimum temperature at which the inclusions might have formed, but depending on entrapment pressure conditions, the actual formation temperatures can be significantly higher.

Salinities were determined using the appropriate phase transition temperature in suitable model geochemical systems, in particular binary (H_2O-NaCl) and ternary (H_2O-NaCl-$CaCl_2$) systems, using the calculations by Steele-MacInnis et al. (2011 and 2012). The choice of model systems was based on the observed microthermometric behavior and phase assemblage. In the binary H_2O-NaCl system, upon heating of a frozen inclusion, the first liquid starts to form at −21.2 °C at the expense of one of the two solid phases forming the eutectic assemblage (ice and hydrohalite, NaCl•2H_2O). Further heating will lead to melting of the remaining solid phase until its temperature of final melting. In the present work, it was common to observe liquid at around −30 °C to −35 °C in the presence of two solids (ice and hydrohalite), which is only possible in a ternary model system, as per the phase rule. The low temperatures at which the first liquid was observed furthermore rules out the system H_2O-NaCl-KCl, because its eutectic is located at −22.9 °C (Sterner et al., 1988). Instead, the presence of divalent cation chlorides such as $CaCl_2$ or $FeCl_2$ is indicated, as these are known to significantly depress ternary eutectic temperatures down to −52 °C (Steele-MacInnis et al., 2011; Lecumberri-Sanchez et al., 2015). Later LA-ICP-MS analyses confirmed the presence of multiple divalent cations. In ternary model systems, salinity can only be determined if two melting temperatures (e.g., ice and hydrohalite) are known. If both transitions were not observable in a given inclusion, the averaged transition temperature from the other inclusions of the same assemblage was used. Finally, for halite-bearing inclusions, salinities were calculated using empirical equations for the halite liquidus in the H_2O-NaCl system (Driesner and Heinrich, 2007; Steele-MacInnis et al., 2012). High-temperature microthermometry was performed after LA-ICP-MS analyses on remaining non-ablated inclusions of the same FIA. This was done to avoid decrepitation and loss of low temperature fluid inclusions during homogenization runs of high temperature assemblages prior to LA-ICP-MS analysis.

3.4. LA-ICP-MS fluid inclusion microanalysis

The LA-ICP-MS analyses were performed at RWTH Aachen University using a Coherent GeoLasHD 193 nm laser ablation system in combination with an Agilent 7900s quadrupole ICP-MS with high-sensitivity s-lens configuration and equipped with platinum sampler and skimmer cones. A small-volume (< 1 cm^3) fast washout ablation cell based on a prototype developed at ETH Zurich was used to ensure highest sensitivities via rapid sample extraction during analysis of the transient fluid inclusion signals. The system was tuned daily to maximize signal-to-background ratios at low oxide (ThO/Th < 0.3%), doubly charged (Ca^{2+}/Ca < 0.25%) production rates and while maintaining stable ablation, transport, and ionization conditions (U/Th = 1.00 ± 0.02). Instrument accuracy for 36 elements was monitored by daily measurements of NIST SRM 612 as a secondary standard prior to analytical runs. The following isotopes were selected for the analyses: ^{7}Li, ^{11}B, ^{23}Na, ^{24}Mg, ^{27}Al, ^{29}Si, ^{34}S, ^{35}Cl, ^{39}K, ^{44}Ca, ^{55}Mn, ^{57}Fe, ^{65}Cu, ^{66}Zn, ^{75}As, ^{85}Rb, ^{88}Sr, ^{107}Ag, ^{118}Sn, ^{121}Sb, ^{133}Cs, ^{137}Ba, ^{182}W and ^{208}Pb. Dwell times of 2 ms were used for all elements, with the exception of Cl where the time was increased to 10 ms. A helium flow of 1.1 l/min was used as carrier gas. For inclusions at moderate depth (>30 μm below the polished surface) a pre-drilling was performed, by creating a conical ablation pit with the purpose of minimizing spallation and cracking of the host mineral, as described in Fusswinkel et al. (2018) and Pettke et al. (2012), before proceeding with the inclusion ablation using a laser repetition rate of 10 Hz. In the case of shallower inclusions, a 5 Hz rate was preferred and predrilling was not done, in order to avoid early opening. For the other instrumental parameters, the routine used by Fusswinkel et al. (2018) was followed.

The raw data was processed with the SILLS software (Guillong et al., 2008) and then manually checked for residual spikes in the signals. NIST SRM 610 was used as the external reference material for all elements, and sample measurements were bracketed by three replicate analyses of NIST SRM 610. Si was selected for the matrix correction for inclusions hosted in quartz and topaz, while Ca was picked for those included in fluorite. Salinities derived from microthermometry were used as input for quantification, and different cation settings were used in the charge-balance based calculations, depending on the chemistry of the fluid (Allan et al., 2005).

4. Results

4.1. Fluid inclusion petrography

Overall, 4 main types of inclusions were observed throughout the samples:

1. Aqueous liquid-dominated, with phase proportions forming a wide spectrum, from around $L_{50}V$ to $L_{95}V$, in primary, pseudosecondary and secondary assemblages depending on the sample. It is the most abundant type in most samples;
2. Vapor-dominated, circa L_5V, present in most samples in different amounts (most abundant in the G3 and G5 granite samples);
3. Brines with only halite as daughter crystal, $L_{85}VH$, present in all samples from this study except those formed in the transitional magmatic-hydrothermal regime (the G5 pegmatite 21MD100I, the G5 miarole LELE and the greisen vein SCH1) and particularly abundant in the granites;
4. Brines with multiple daughter crystals, $L_{85}VHX+$, observed in the same samples as the type 3 brines, but generally less abundant and rarely forming clear FIAs.

With the exception of CO_2-bearing fluid inclusions that were not spotted in the present study, these types coincide with those listed in previous studies of this type conducted across the Cornubian batholith (Alderton and Rankin, 1983; Rankin and Alderton, 1983; Jackson et al., 1989). In the following sections a more detailed report of the fluid inclusion types distribution for each specimen is presented.

4.1.1. Granite samples

Sample 21MD1 consists of a biotite-rich granite (G3), with pluricentimetric K-feldspar phenocrysts, whereas 21MD219 represents an equigranular topaz-bearing granite (G5). In both rocks, quartz is always interstitial and anhedral, resulting in a lack of growth features that would enable identification of primary FIA. Pseudosecondary FIAs in trails that begin and terminate entirely within an individual grain do occur but are relatively rare (Fig. 3a). The topaz in the G5 granite sample 21MD219 forms plurimillimetric crystals are either isolated or surrounded by later quartz. Topaz contains abundant mineral inclusions, such as albite, lepidolite and tourmaline. In some topaz grains, pseudosecondary trails of liquid-dominated type 1 aqueous inclusions are found (Fig. 3f), whereas brines and vapor-dominated inclusions (types 2–4) are entirely absent. Conversely, the later quartz contains type 3 and type 4 fluids respectively with one (e.g., Fig. 3b) or more daughter crystals (up to 4–5 different solids), as well as type 1 and 2 aqueous FIAs. Likewise, the G3 granite sample is also characterized by brines (type 3

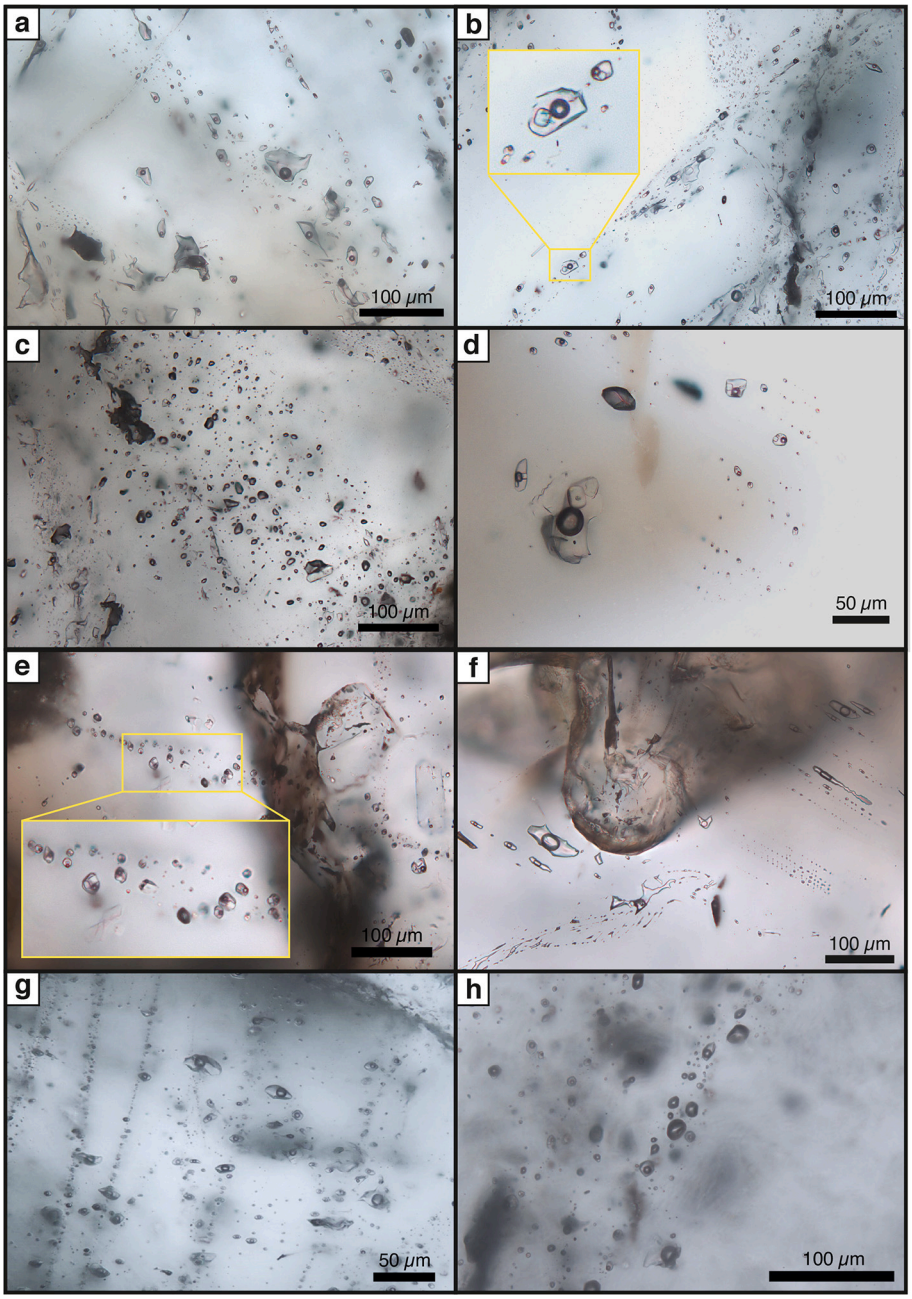

Fig. 3. Microphotographs of specimen 21MD1 (a-d), 21MD219 (e-f) and 21MD222 (g-h) showing representative types of FIAs. a) pseudosecondary trail of $L_{85}V$ inclusions (type 1); b) secondary brine trail with consistent phase proportions $L_{85}VH$; c) planar arrangement of vapor-dominated inclusions (L_5V); d) pseudosecondary planar arrangement consisting of mainly brines $L_{85}VHX+$ intercalated with vapor-dominated L_5V inclusions following the same alignment: this represents an example of boiling trail; e) secondary trail containing $L_{85}VHX+$ brines intercalated by L_5V, representing a boiling assemblage; f) pseudosecondary liquid-dominated $L_{80}V$ inclusions hosted in topaz; g) secondary $L_{85}V$ trails subparallel to the vein borders particularly abundant in combed quartz growing from the vein margin; h) boiling assemblage featuring $L_{85}V$ and L_5V inclusions in latest quartz at the vein center.

and type 4) hosted in quartz, as well as liquid-rich and vapor-rich fluids (type 1 and type 2). Vapor-dominated type 2 inclusions (L_5V) typically form homogeneous clusters, but also planar arrangements (Fig. 3c). In quartz from both samples, rare boiling trails with coexisting halite-bearing brines and vapor-dominated inclusions were observed (Fig. 3d, e).

Sample 21MD222 is a quartz-only vein cutting through the G5 granite, and collected in the same locality as sample 21MD219 (Rostowrack pit, St. Austell). Context and paragenesis suggest a late-magmatic to early hydrothermal origin, confirmed by later high-temperature microthermometry. The vein filling consists of euhedral to subhedral quartz grains, followed by a layer of quartz containing tufts of acicular "hair-like" tourmaline and then typically wrapped in a chalcedony layer near the rim. $L_{85}V$ type 1 fluids predominate (Fig. 3g), but vapor-rich L_5V type 2 fluids are common as well. Type 3 fluids are rare and typically present as isolated inclusions rather than trails; only very few inclusions with more than one daughter crystal (type 4) were spotted. Most of the selected FIAs are pseudosecondary trails that do not

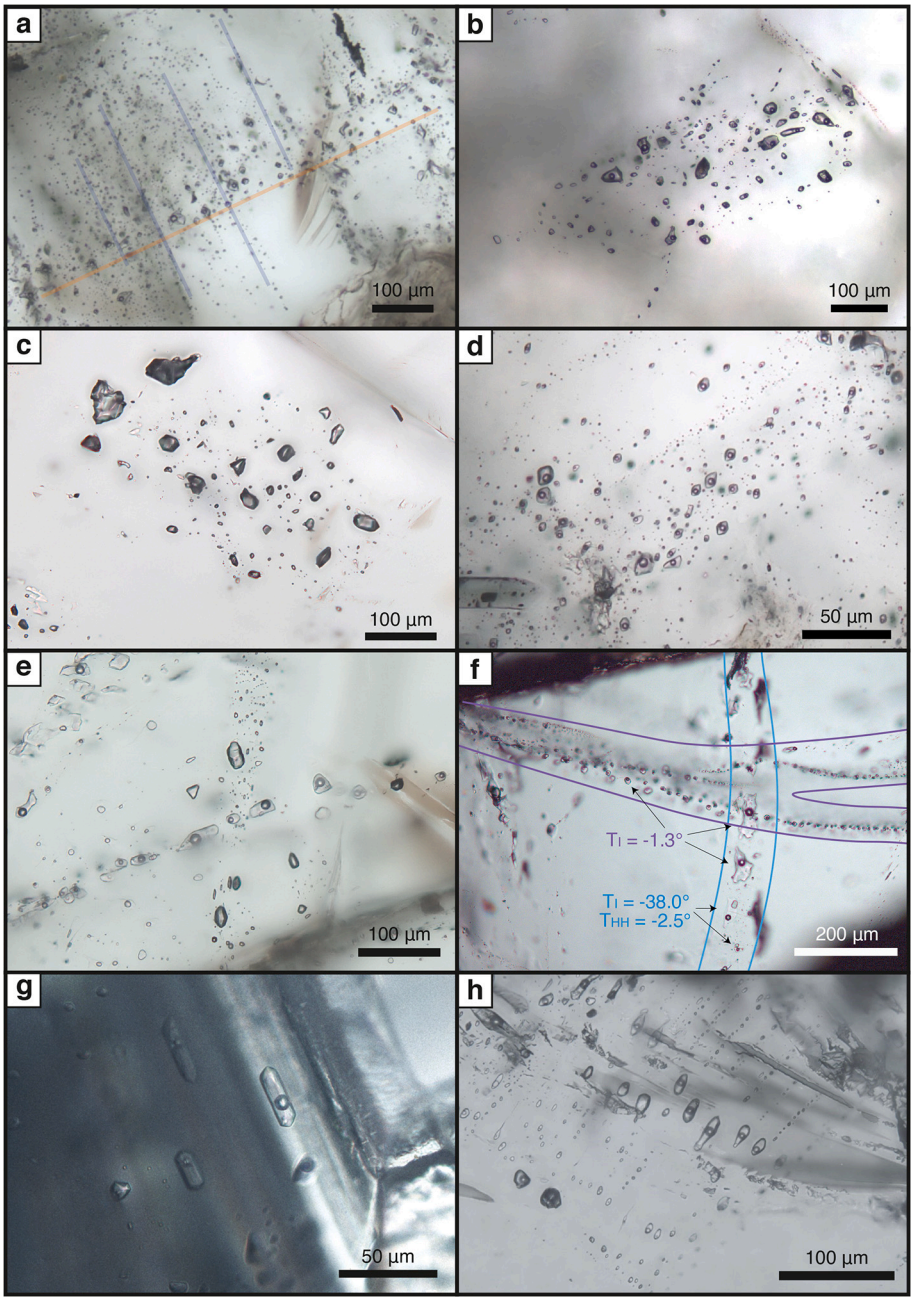

Fig. 4. Microphotographs of samples 21MD100I (a), LELE (b-c), SCH1 (d), 21MD65 (e-f), 21MD10S (g), 21MD10B (h): a) intersection between the two main sets of trails in sample 21MD100I, with the subhorizontal set (highlighted in orange) forming fewer trails but with bigger inclusions size consistently across the whole section; b) pseudosecondary trails of $L_{85}V$ inclusions, very common in the central part of the euhedral crystal; c) cluster of vapor-dominated L_5V inclusions, not uncommon in sample LELE; e) intersection between a vapor-dominated FIA (L_5V) and several $L_{85}V$ trails, although the relative time relationships are difficult to assess; f) cross-cutting trails, with an older brine FIA ($L_{90}VH$, in blue) cut by a later low salinity $L_{85}V$ FIA (in violet), as indicated by the large inclusions at the intersection which maintained the inclusion shape and size of the older brines trail but the fluid content was replaced during the emplacement of the $L_{85}V$ trail, as shown by the microthermometry data. Abbreviations: T_I - ice melting temperature; T_{HH} - hydrohalite melting temperature; g) primary $L_{90}V$ inclusions following quartz zoning; h) example of pseudosecondary FIA of $L_{90}V$ type. (For interpretation of the references to colour in this figure legend, the reader is referred to the web version of this article.)

extend into the late tourmaline-bearing and chalcedony layers. Rare primary trails mimicking the crystal zoning are present and they contain liquid-dominated aqueous type 1 inclusions. Within individual quartz grains, relative ages between FIAs can be established. Type 3 brines and type 2 L_5V tend to be early, whereas type 1 aqueous $L_{85}V$ fluids cover the entire time span, indicating early or episodic boiling to have occurred in a system otherwise dominated by single-phase fluids. The type 3 brine inclusions are never associated with the isolated type 2 vapor-rich L_5V inclusions, although both types occur only near the vein margin in close spatial proximity and are thus interpreted as boiling assemblages, although no direct petrographic evidence exists. A few secondary assemblages in very late quartz grains in the center of the vein filling contain vapor-rich inclusions (also ca. L_5V) coexisting with aqueous $L_{90}V$ inclusions. Later microthermometry revealed the latter to be of high salinity, indicating these assemblages to also represent boiling conditions (Fig. 3h).

4.1.2. G5 pegmatite and miarolitic cavity

The pegmatitic/miarolitic samples 21MD100I and LELE, representing the magmatic-hydrothermal transition, were both collected from the G5 stock of Tregonning-Godolphin, the former in the eastern part (Megiliggar Rocks) in sills branching from the granite cupola into the country rock, and the latter in a miarolitic cavity in the western part of the stock (Lesceave Par). 21MD100I was taken from a locality characterized by alternating pegmatitic and aplitic layers, already subject of numerous studies (e.g. Stone, 1969, 1992; Breiter et al., 2018). In the pegmatitic parts UST textures are common, with combed K-feldspars growing inward and quartz in interstitial position. LELE, on the other hand, represents an open cavity where quartz could grow with a euhedral habit.

The fluid inclusion record of the pegmatitic UST section (21MD100I) displays two sets of secondary fluid inclusion trails with distinct orientations (Fig. 4a). The first set is strongly predominant and occurs subperpendicular to the K-feldspar phenocrysts, while the less common second set is oriented subparallel to them. Petrographically they are very similar, with both sets containing aqueous type 1 $L_{85}V$ inclusions. Vapor-dominated type 2 inclusions are present but rare, and no brine inclusions with daughter crystals (type 3 or type 4) were observed.

The euhedral quartz in sample LELE shows clear growth zoning, making it possible to firmly establish temporal relationships between fluid inclusion assemblages. Petrographically, the core of the pluricentimetric crystal is characterized by several dense clusters of liquid-dominated aqueous type 1 inclusions, while the outer parts of the crystal are much clearer. Here, abundant primary FIAs of type 1 have markedly smaller fluid inclusions sizes of <5 μm, too small for LA-ICP-MS. Therefore, only pseudosecondary FIAs were selected for further analysis (Fig. 4b), but the clear growth zoning of the sample still permits to place those in a rigid temporal framework. Similar to the pegmatite sample, the miarolitic quartz is overall strongly dominated by aqueous type 1 $L_{85}V$ fluids with minor occurrences of type 2 vapor-dominated FIAs (Fig. 4c), while LVx type inclusions (types 3 and 4) were not observed at all. Finally, the entire crystal is rimmed by a thin layer of chalcedony.

4.1.3. Sn—W greisen and Sn-Cu-As polymetallic mineralization

SCH1 features an endogranitic quartz vein with minor arsenopyrite with a greisen border from Cligga Head, where a large Sn- and W-rich sheeted-vein complex was mined in the past. Mineralization commonly occurs in patches of cassiterite, wolframite, arsenopyrite, chalcopyrite in the center of the veins, with variable width of the greisenized halo, however, the selected specimen only contains minor arsenopyrite. The anhedral vein quartz features densely spaced pseudosecondary and secondary FIAs on healed fractures. This, and the absence of clear growth features in the anhedral quartz grains, make it impossible to establish textural context and temporal relationships between different FIAs. Similar to the G5 pegmatite sample (21MD100I), there is a predominant orientation of fluid inclusion trails, subperpendicular to the vein border, but not as clear as in 21MD100I (Fig. 4d). $L_{85}V$ type 1 fluids are by far the most common fluid type, but some minor vapor-dominated type 2 fluids and rare aqueous $L_{50}V$ FIAs can be observed. Fluid types 3 and 4 were not observed, but many inclusions show signs of accidental entrapment of muscovite flakes.

The specimen 21MD65 from Botallack (Land's End pluton) consists of a vein perpendicular to the (G4) granite-country rock contact. It contains fluorite, chalcopyrite, chlorite and arsenopyrite. The country rock is a chlorite-dominated greenstone. Chlorite is abundant also within the vein, where it occurs as spherical aggregates of acicular crystals. Arsenopyrite is found mainly at the edges of the vein, while fluorite and chalcopyrite fill the central part. Close to the contact with the vein and the country rock, the granite contains abundant chalcopyrite and arsenopyrite, whereas fluorite is absent. Granite-hosted magmatic quartz contains liquid-rich type 1 ($L_{85}V$), vapor-rich type 2 and halite-bearing type 3 fluid inclusions, but the trails are often very short and FIAs were difficult to define unambiguously, especially due to the small grain size of quartz, and therefore these FIAs were not used for subsequent analyses. In the vein, fluorite hosts mainly type 1 aqueous $L_{85}V$ (Fig. 4e, f) and halite-bearing $L_{90}VH$ brine inclusions (type 3, Fig. 4f) and only minor type 2 L_5V trails (Fig. 4e). The overall abundance of fluid inclusions is significantly lower than in the magmatic quartz, and FIAs in healed fractures are exceptionally well preserved. Cross-cutting relationships and replacement features indicates the liquid-dominated type 1 fluid to postdate the halite-bearing fluid (Fig. 4f). The inclusions at the intersection, in fact, have the morphology and orientation of the brine inclusions, but contain the low salinity type 1 fluid as replacement, indicating that the latter formed at a later stage.

Sections 21MD10S and 21MD10B were cut from the same specimen of an endogranitic vein from Birch Tor, hosted in the G3 Dartmoor granite. The vein shows evidence for multiple cycles of reactivation and mineral precipitation. This feature has been described from this locality before, and previous studies established the following paragenetic sequence for veins and vein infill mineralization from oldest to youngest: 1) tourmaline-only; 2) tourmaline-quartz-cassiterite; 3) quartz-hematite; 4) quartz-only (Scrivener, 1982). The collected sample record the episodes number 2 and 3, and cross-cutting relationships confirm the temporal sequence between the two.

Sample 21MD10S contains one vein for each of the two episodes subparallel to each other, plus a subordinate veinlet of stage 3 quartz-hematite cutting through the tourmaline-bearing stage 2 vein. Fluid inclusions in the stage 2 vein are rarely forming well-defined trails and despite being dominated by the liquid-rich $L_{85}V$ type 1 fluids, vapor rich type 2 (L_5V) and halite-bearing type 3 inclusions ($L_{85}VH$) are common. No FIAs were found in the stage 2 vein, due to the abundance of fine-grained tourmaline and an overall lack of clear fluid inclusion trails. In the larger quartz crystals in the quartz-hematite vein, on the other hand, the fluid inclusion record is clearer and unambiguous. The hematite-bearing vein hosts predominantly liquid-dominated type 1 $L_{90}V$ inclusions, with similar abundance of vapor-dominated (type 2) but significantly fewer type 3 halite-bearing inclusions than in the stage 2 tourmaline-bearing quartz vein. Vapor-dominated inclusions typically occur in homogeneous trails but few instances of co-existence with high salinity liquid-dominated inclusions (boiling trails) have been observed. Some primary and pseudosecondary trails are present and they typically contain only type 1 $L_{90}V$ inclusions (Fig. 4g).

Sample 21MD10B contains a large quartz-hematite vein of ca. 3 cm width, containing at least two generations of quartz: the earlier consists of euhedral crystals growing inwards from the vein edge and is separated from the later subhedral quartz by a layer of chalcedony. The early quartz contains abundant aqueous type 3 and 4 brine FIAs with one (halite) or more daughter crystals, as well as subordinate amounts of aqueous type 1 $L_{85}V$ and L_5V vapor-rich FIAs with similar abundances between the two types. The later quartz is strongly dominated by liquid-rich type 1 $L_{90}V$ inclusions, while type 2 (L_5V) and type 3 ($L_{85}VH$) FIAs

are rare. In some instances, especially in the later generation of quartz, a crystal zoning is evident and fluid inclusions (primary FIAs) follow this zoning, allowing to put them in a defined temporal framework. In addition, pseudosecondary trails are abundant throughout the section (Fig. 4h). In analogy to sample 21MD10S, these growth features and healed fractures contain mainly type 1 $L_{90}V$ inclusions.

4.2. Microthermometry

A total of 1120 inclusions in 277 FIAs were analyzed by microthermometry. Only FIAs with consistent microthermometric properties were subsequently used for LA-ICP-MS analysis, and fluid types not forming clear trails were not analyzed. Around 90% of the FIAs were aqueous liquid-dominated inclusions between $L_{95}V$ and $L_{75}V$ of type 1, while the remaining were halite-bearing aqueous liquid-dominated inclusion (averaging $L_{85}VH+$) containing one (type 3) or more daughter crystals (type 4; up to 4–5 different solids in a few cases, normally 2 or 3).

Microthermometry of the low-density vapor-rich L_5V type 2 inclusions occurring in samples from all stages was complicated by their small sizes and the very small proportion of liquid, often precluding unambiguous observation of phase transition temperatures. Consequently, their salinity is difficult to estimate and their compositional data has to be considered qualitative at best. In the few instances analyzed via LA-ICP-MS, Na was the only element consistently above the limit of detection and no further geochemical data from this type of inclusions are presented.

4.2.1. Salinity variations

Most samples contain fluid inclusion types spanning a wide compositional range, with granite-hosted FIAs in samples 21MD1 (G3 granite) and 21MD219 (G5 granite) reaching salinities over 40 wt%, while in most other samples salinities range from ca. 25 wt% to <1 wt% $NaCl_{eq}$ (Fig. 5). The only exception is the G5 pegmatite in which only relatively lower salinity fluids occur (< 7.5 wt% $NaCl_{eq}$). Some samples cover the salinity range continuously (e.g., 21MD1, G3 granite), whereas others record discrete fluid pulses of variable salinity, with slight salinity changes during the early magmatic evolution, before decreasing in the latest fluids (Fig. 5). In general, aqueous type 1 fluids hosted in quartz show systematic decrease in salinity paired with decreasing homogenization temperature accompanied by a decrease in vapor phase proportion in progressively younger FIAs.

A clear example of decrease of salinity with time is the fluorite-arsenopyrite-chalcopyrite vein sample (21MD65), where type 3 high-salinity brines, as well as two populations of aqueous liquid-dominated type 1 fluids of different salinities occur (Fig. 5). Crosscutting relationships (see section 4.1.3 and Fig. 4f) show that the high salinity brine predates a low-salinity fluid (~2.2 wt% $NaCl_{eq}$). A second aqueous fluid possesses intermediate salinities (~14 wt% $NaCl_{eq}$, Fig. 5), but unfortunately no clear time relationship with the other two could be established during fluid inclusion petrography because this fluid type is quite uncommon. High-temperature microthermometry, however, revealed an intermediate homogenization temperature (~296 °C) of the intermediate salinity fluid type with respect to the low-salinity (~226 °C) and the high-salinity (>330 °C) fluids, indicating that it is temporally intermediate between the high and low salinity fluids.

In sample 21MD10B (Hem-Qtz vein in G3 granite), it is important to note that the type 3 and 4 brines mentioned in section 4.1.4 do not form well-defined FIAs and are therefore excluded from further analysis. Among the aqueous type 1 FIAs, salinities forming a continuous compositional array ranging from 25.2 to 0.4 wt% $NaCl_{eq}$ without forming discrete populations (Fig. 5). Highly saline aqueous FIAs occur almost exclusively in the first quartz generation (similarly to the brines), while the second quartz generation is dominated by low salinity inclusions, with a minor presence of high salinity FIAs (Fig. 6). While the presence of the later low salinity fluids as secondary FIAs in early quartz is to be expected, the occurrence of high salinity fluids in later quartz shows that the general trend towards lower salinities during vein formation was interspersed by episodic flow events involving higher salinity fluids.

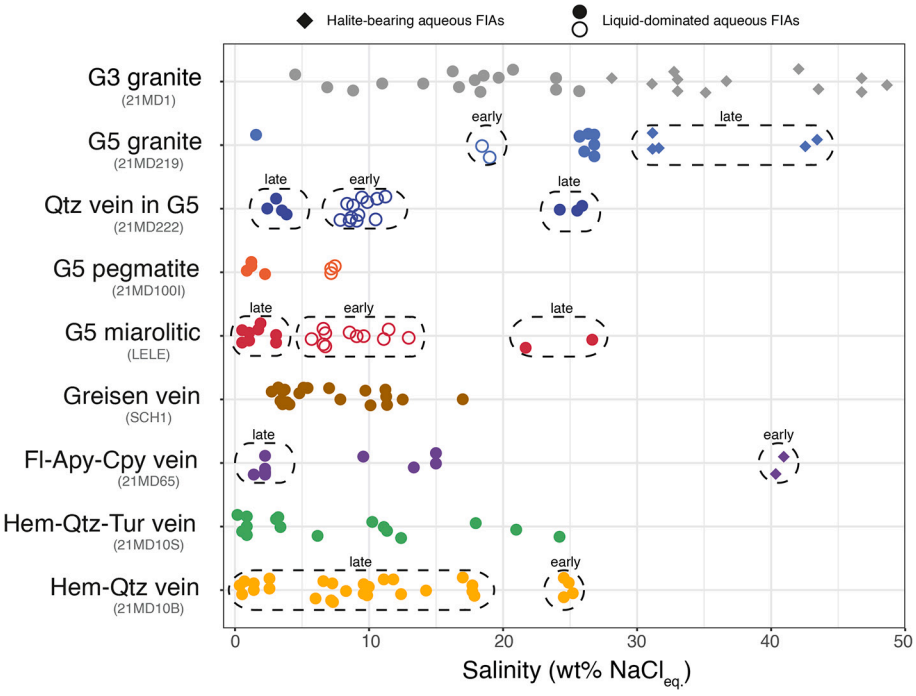

Fig. 5. Summary of the fluid inclusion assemblage salinities (average) for each sample. The diamond shape indicates the assemblages where one or more daughter crystals are present at ambient conditions (brines), whereas all the others represent LV-type inclusions (liquid-dominated; refer to the discussion for the difference between open and filled circles). The standard deviation of the salinity for each FIA is smaller than the symbol size. Vapor-dominated inclusions are not plotted and have a ubiquitous salinity of 0.1 ± 0.1 wt% $NaCl_{eq}$. Where known, relative age relationships of the different salinity groups are indicated (with dashed contours).

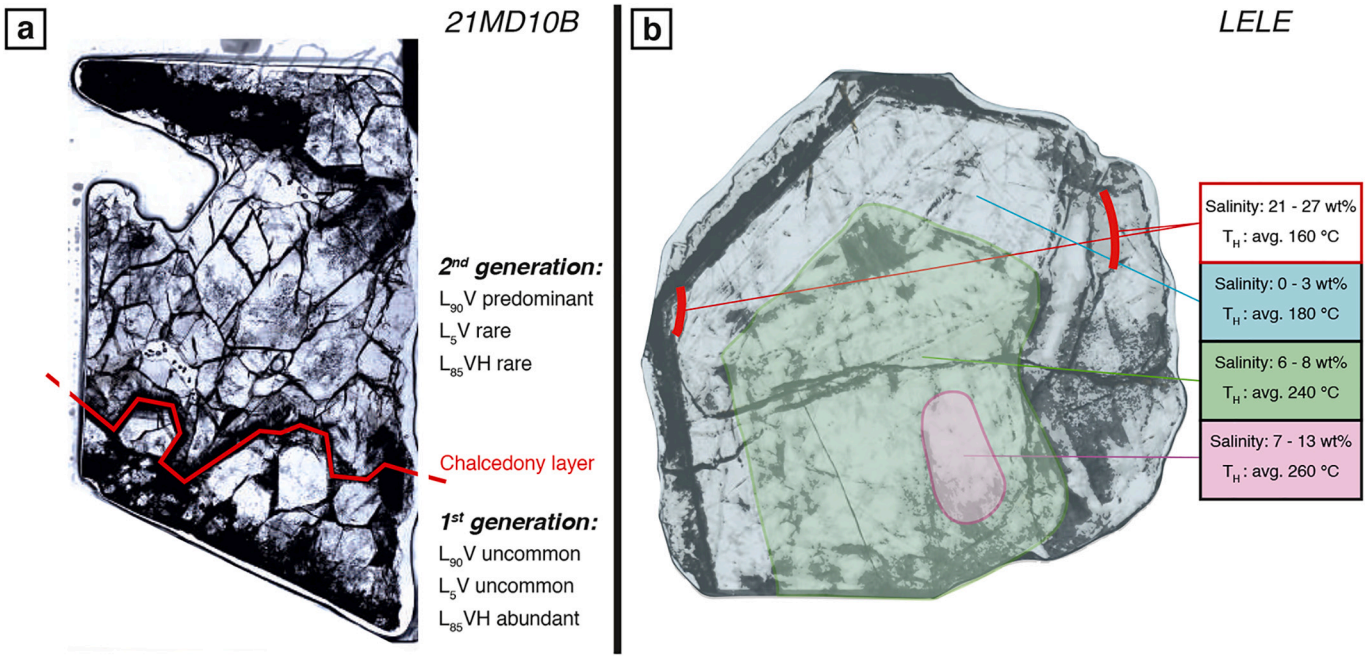

Fig. 6. Sections overview highlighting quartz textures and fluid inclusions distribution. a) Sample 21MD10B characterized by two generations of quartz separated by a chalcedony layer; the frequency of brines significantly decreases from the first to the second quartz generation. b) Sample LELE with three main zones (core in pink, edge in green and rim in turquoise) showing a progressive decrease in salinities and homogenization temperatures from core to edge, with the exception (for salinity) of the trails marked in red. (For interpretation of the references to colour in this figure legend, the reader is referred to the web version of this article.)

The G5 miarolitic cavity sample (LELE) consisting of a pluricentimetric euhedral zoned quartz, displays an overall consistent trend of progressive decrease in salinity from the core towards the crystal edge (Fig. 6). However, a few secondary trails are characterized by high salinity inclusions, with salinities of 21.7 and 26.7 wt% $NaCl_{eq.}$. They don't contain halite at ambient conditions ($L_{90}V$), but they will be referred as brines in the following chapters, as they are significantly more saline than the rest of the FIAs in the sample. High-temperature microthermometry revealed that homogenization temperatures decrease unequivocally from core to rim and adjacent high and low salinity inclusions trails in the crystal edge recorded similarly low homogenization values (Fig. 6).

In the remaining sections, a lack of growth zones or clear crosscutting features precluded placing the pseudosecondary FIAs within a relative temporal framework. In the G5 pegmatite (21MD100I) two main sets of trail orientations exist (Fig. 4a). Microthermometry shows a bimodal distribution of salinities, with a group of around 7 wt% salinity and another ranging between 2.2 and 0.9 wt% $NaCl_{eq.}$. They homogenize at temperatures around 320 °C, and 230 °C respectively. Both these fluids occur in both principal fracture orientations, therefore no further textural discrimination is possible. Similarly, in the greisen vein (SCH1) two sets of orientations were noted (Fig. 4d), likewise without a correlation with salinity, which in this case forms a continuous array between 17 and 2.7 wt% $NaCl_{eq.}$. In this sample, FIA trails comprise 5–6 inclusions at best, resulting in only few inclusions being available for high temperature microthermometry after LA-ICP-MS, therefore the results are limited to overall geochemistry and no clear trend with respect to homogenization temperatures was observed.

In the G5 quartz vein (21MD222), several grains show a consistent trend of decreasing salinity from the core to the rim of the crystals in the intermediate and low salinity aqueous type 1 fluids, ranging from 11.2 wt% to 3.5 wt% $NaCl_{eq}$. Similarly, homogenization temperatures decrease from core to rim within crystals from 390 °C to 250 °C. This indicates that the different quartz grains of the vein infill were formed during a single continuous event. Only the very latest quartz grains at the center of the vein record the existence of late boiling assemblages containing high salinity inclusions coexisting with vapor-rich inclusions (Fig. 3h). Similarly, in the quartz-hematite vein in 21MD10S, it is difficult to establish time relationships between different crystals. Nevertheless, primary and pseudosecondary trails define a temporal framework valid for individual grains, and homogenization temperatures record a limited range (from 240 to 350 °C) without a clear correlation with salinity, which in this case forms a continuous array from around 24 wt% to below 0.5 wt% $NaCl_{eq.}$.

4.2.2. *Homogenization behavior of brine inclusions*

The two granite samples (21MD1, G3 granite and 21MD219, G5 granite) both contain high-salinity brine FIAs showing two types of total homogenization behavior. Some inclusions homogenize via liquid-vapor homogenization after halite dissolution (LVH- > LV- > L), while others homogenize via halite dissolution after vapor disappearance (LVH- > LH- > L), in concordance with previous fluid inclusions studies on the Land's End pluton (Müller et al., 2005). Brine FIAs occur either in boiling assemblages coexisting with vapor-dominated inclusions or forming distinct homogeneous FIAs with consistent phase proportions. Their homogenization via halite dissolution points to some degree of post-entrapment modification, as brine inclusions formed via fluid phase separation must homogenize via liquid-vapor homogenization. Audétat (2022) found that post-entrapment effects such as shrinkage of fluid inclusions and concomitant water loss can cause such changes in homogenization behavior. Salinities derived from halite dissolution temperatures in such cases can then be subject to overestimation. Fig. 7 shows liquid-vapor homogenization temperatures (T_HL-V, Fig. 7a) and total homogenization temperatures ($T_H$tot, Fig. 7b) plotted against fluid salinity. Inclusions homogenizing via halite dissolution plot above the halite liquidus in Fig. 7a. This allows to visualize which FIAs have possibly undergone post-entrapment modifications as they plot above the halite saturation curve in Fig. 7a.

4.3. *LA-ICP-MS results*

A total of 165 FIAs were successfully characterized with LA-ICP-MS

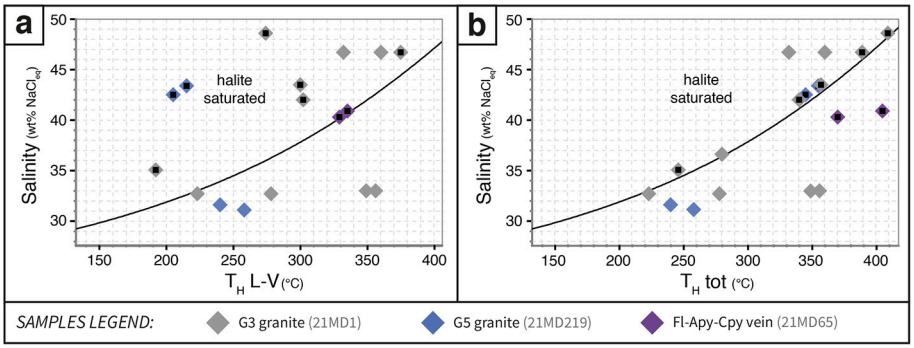

Fig. 7. Diagram showing salinity vs a) liquid-vapor homogenization temperature; b) final homogenization temperature for brines of different samples. The points differing between the two diagrams (marked with a black square) represent the FIAs that homogenized at last via halite dissolution.

analysis. The results presented here include relative compositional comparisons between fluid chemistries from different intrusive centers and magmatic-hydrothermal stages. It is important to highlight that, although the batholith is thought to have a single deep magma reservoir, spatially discrete events, such as the emplacement of discrete plutons, and significant temporal differences exist between magmatic and hydrothermal events across the region. Therefore, the comparisons of relative element concentrations cannot be considered representative of the development of the entire batholith system, but instead only serve to illustrate the most striking compositional differences between the samples studied here. Detailed discussion and comparison of compositional trends from individual subsystems will be provided below. The complete dataset is available in the supplementary material, which includes also the data from microthermometry.

4.3.1. *Major elements*

The dominant cation in almost all studied fluids is Na, with subordinate amounts of K and Ca (Figs. 8, 9). The proportions between these main cations are very consistent within individual fluid inclusion assemblages, but vary significantly within and between samples (Fig. 8). Notably, fluids hosted in G3 granite (21MD1, Dartmoor pluton) are distinctly more Ca-rich than all other fluids, while G5 granite-related fluids (21MD219) are Ca-poor, forming a cluster separate from the concentration ranges observed in all other fluids (Fig. 8). The Ca enrichment in the Dartmoor granite in comparison with the other plutons was also observed by Rankin and Alderton (1985), although from

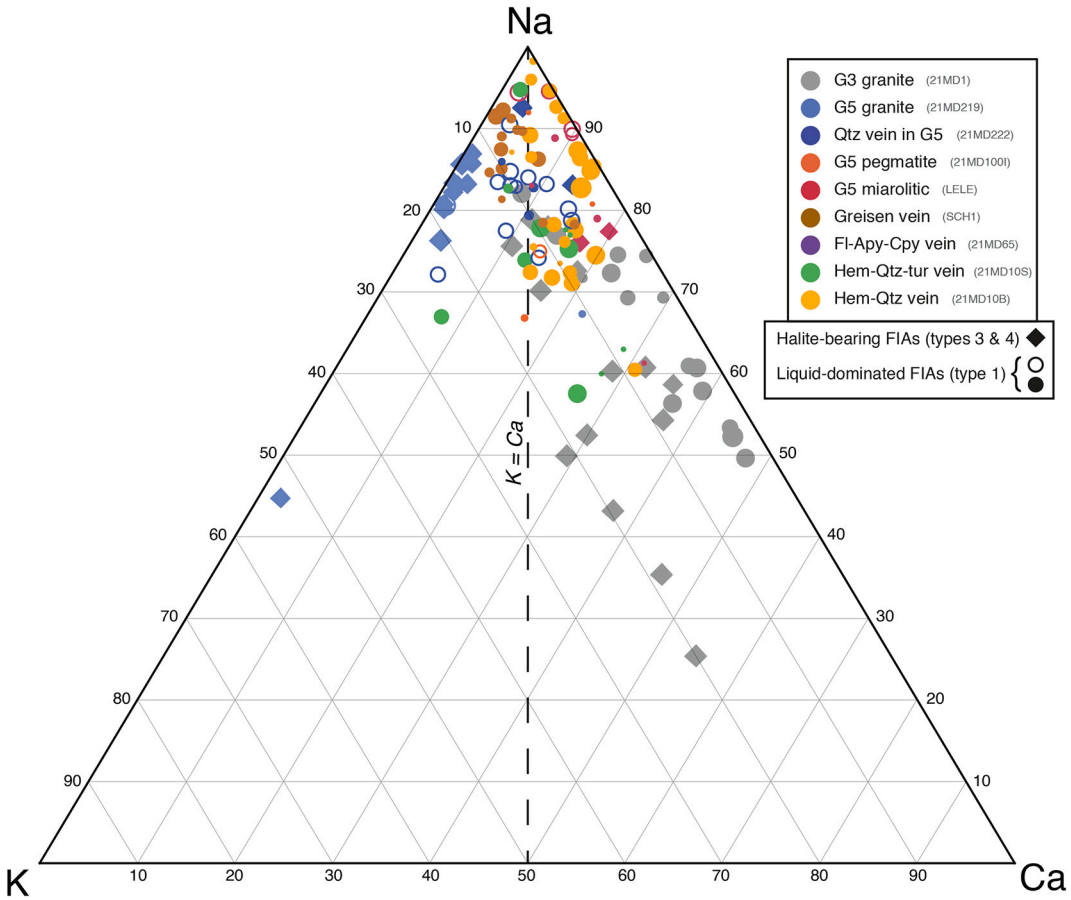

Fig. 8. Ternary diagram of molar concentrations of the main cations (Na, Ca and K) determined by LA-ICP-MS analysis. All points represent FIA averages and symbol size is proportional to salinity (higher salinities – larger symbols). The dashed line represents the K/Ca ratio of 1. Abbreviations: Qtz - quartz; Fl - fluorite; Apy - arsenopyrite; Cpy - chalcopyrite.

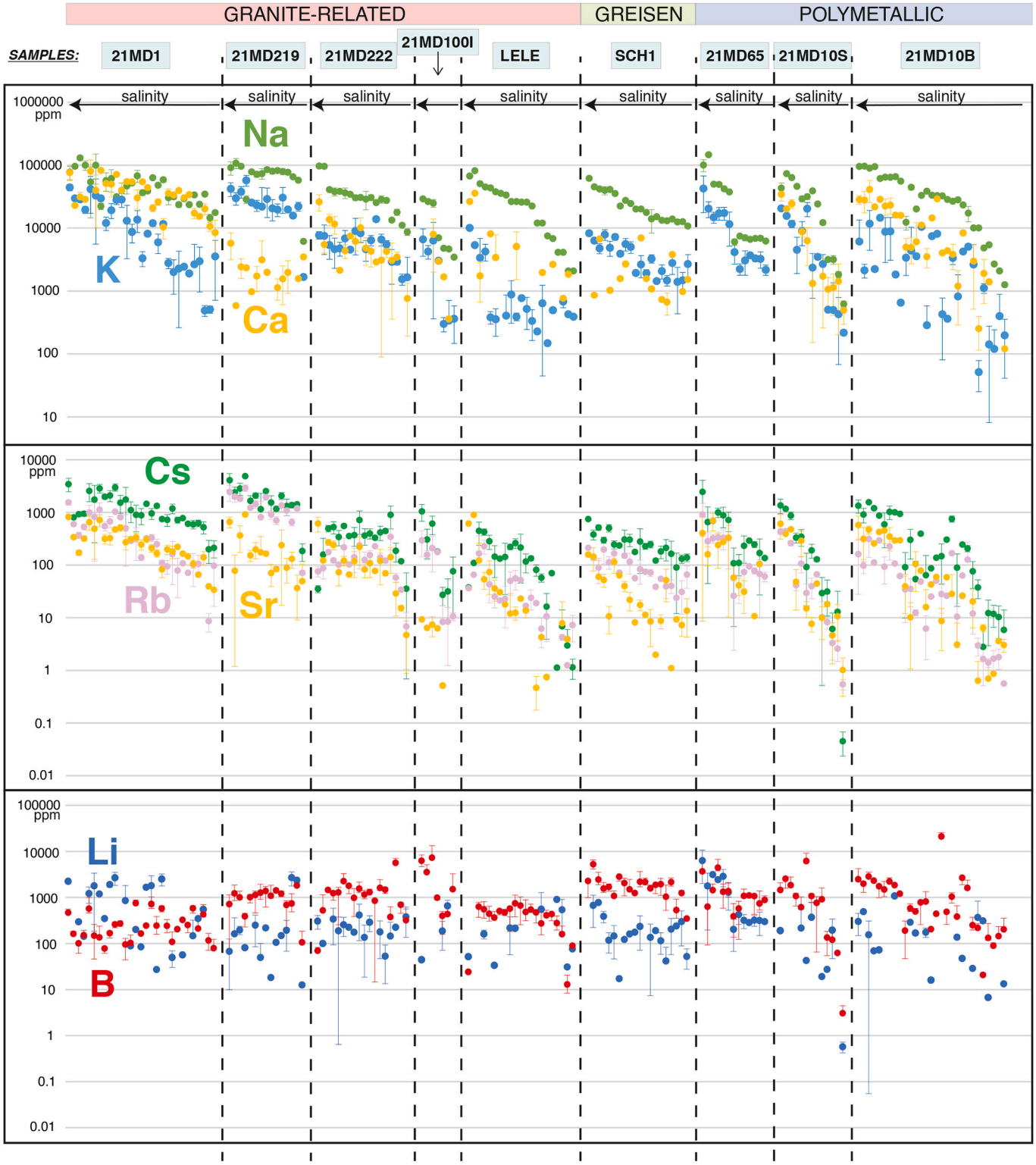

Fig. 9. Major, minor and trace elements concentrations of FIAs (averages) from LA-ICP-MS analysis (in ppm). The data is divided by sample, and within each sample FIAs are ordered from high to low salinity (see arrows). The bars represent the standard deviation for each FIA.

bulk fluid inclusions geochemistry. The late magmatic to hydrothermal samples show a relatively large scatter in the ternary diagram (Fig. 8), but mostly plot at K/Ca ratios intermediate between the two granites, and slightly higher Na. In sample 21MD1, the FIAs affected by post-entrapment modifications (chapter 4.2.2) have relatively high apparent K/Ca ratios compared to the rest of the sample.

In light of the overall heterogeneity in the major cation concentrations between samples, the minor and trace elements shown in the following chapter are presented normalized to Cl rather than to Na, as the former correlates better with the overall salinity of the fluids.

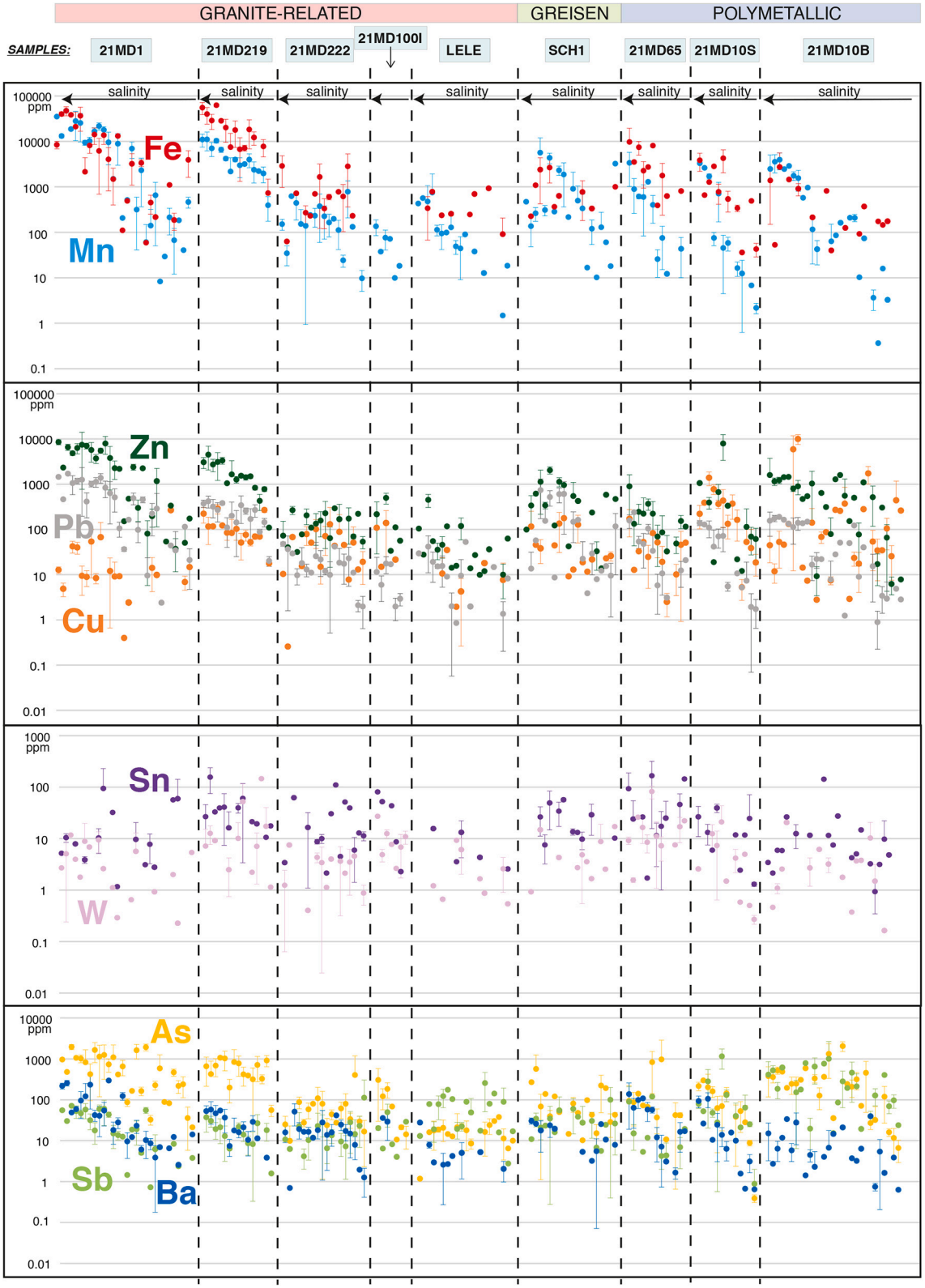

Fig. 9. (*continued*).

4.3.2. Minor and trace elements

Cesium, Rb and Sr have concentrations well above detection limits in all the fluids, with concentrations between 10 ppm and 1 wt% (Fig. 9), positively correlated with salinities. The strong Rb enrichment in whole rock data for the G5 granite reported by Simons et al. (2016), was partly observed also in the related fluids in sample 21MD219, and it correlates with higher values of Cs too (compared to G3 fluids in 21MD1). Rb/Cs ratios are typically <1 and very similar across all the samples and fluid types. The only exceptions are the G5 granite fluids, characterized by the aforementioned high-Rb anomaly resulting in Rb/Cs = 1 (Fig. 10a). Sr overall correlates with the two alkali elements, but show a marked depletion in the G5 pegmatite fluids (21MD100I) (Fig. 10b), in

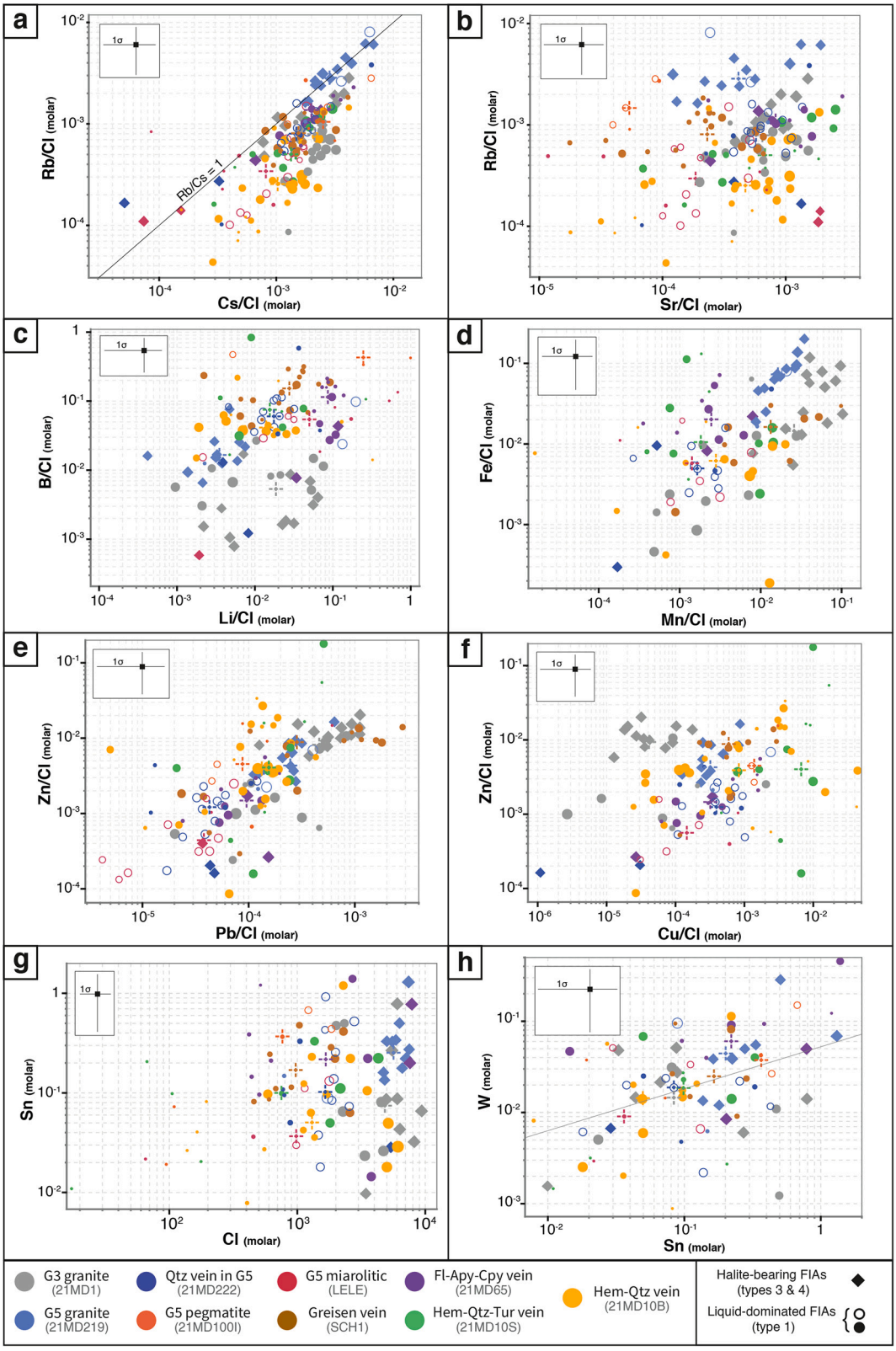

Fig. 10. Comparison of minor and trace elements data from LA-ICP-MS in Cl-normalized diagrams (except g and h). All points represent FIA averages and symbol size is proportional to salinity. Dashed crosses represent median values for each sample. In a, the line of Rb/Cs = 1 is displayed for clarity. In h, the overall regression line is shown. The median relative error is shown for each diagram. See discussion for the distinction between open and filled circles.

agreement with the whole rock geochemistry from this area (Breiter et al., 2018).

Lithium and B concentrations typically range from 50 to 5000 ppm in all studied fluids (Fig. 9), with an overall weak correlation with salinities. The highest Li concentrations are found in early granitic fluids (particularly 21MD1, G3 granite) and the fluorite bearing vein sample (21MD65), hosted in G4 granite. G3 granitic fluids are the only ones in which Li contents systematically exceed B concentrations in the high salinity FIA, while the opposite is true for all other studied fluids (Fig. 9). In the greisen sample (SCH1, hosted in G2 granite) and late-stage quartz-hematite veins (21MD10S, 21MD10B, hosted in G3 granite), B exceeds Li concentrations by almost an order of magnitude. In the remaining samples, concentration differences are smaller, but are nevertheless typically characterized by B > Li. Chlorine normalized element ratios show that late magmatic and hydrothermal fluids form a relatively consistent compositional array in B/Cl – Li/Cl space (Fig. 10c). Interestingly, lower salinity G3 granite fluids (21MD1) also cluster within this group, while higher salinity fluids in the same sample have significantly lower B/Cl and form an offset compositional trend. The late-stage fluorite-arsenopyrite vein fluids (21MD65) are similarly shifted towards higher Li/Cl ratios. G5 granitic fluids (21MD219) form part of the main compositional array, but possess the lowest Li/Cl and B/Cl values (Fig. 10c). This observation is in opposition with the whole rock geochemistry of the two granitic samples, in particular for G5 granite, where the highest magmatic Li contents are observed (Simons et al., 2017). However, G5 pegmatite fluids (21MD100I) have the highest values for both B/Cl and Li/Cl.

Manganese and Fe show concentrations with large ranges (from few ppm to around 0.5 wt%) that strongly correlate with inclusion salinity. Both elements are present in significantly higher concentrations in granite-related fluids in comparison with the rest of the sample set, and within the same order of magnitude for the two elements (Fig. 9). Notably, in G5 pegmatite fluids, Fe is always below the limit of detection. This Fe depletion is in agreement with the whole rock data by Breiter et al. (2018) of the most fractionated G5 melts around Megiliggar Rocks (Tregonning-Godolphin stock), which is also the provenance of the sample studied here. Mn/Cl is highest in granitic fluids and it is moderately high for the greisen vein (SCH1), compared to the rest (Fig. 10d). Similarly, Fe/Cl is highest in G5 granite fluids. All studied fluids form a relatively tight compositional array in Fe/Cl – Mn/Cl space (Fig. 10d).

Lead and Zn show an overall good correlation with salinity and between them (Fig. 9). On the other hand, Cu seems less correlated with salinity. In Cl-normalized diagrams the granite fluids (21MD1, 21MD219) show the highest Pb/Cl and Zn/Cl values, together with the greisen fluids (SCH1), which is particularly enriched in both metals (Fig. 10e). In contrast, Cu/Cl shows only a moderate correlation with Zn/Cl for some samples, while other fluids (particularly G3 granite-related fluids in 21MD1) are significantly offset towards lower Cu/Cl ratios, or higher ones in the case of the late Hem-Qtz-Tur vein (21MD10S) (Fig. 10f).

Tin and W content show a limited range of concentrations, mostly between 1 and 100 ppm (Fig. 9), with no systematic correlations with salinity (Fig. 9, 10f), proximity to the mineralization, or between magmatic, late-magmatic and hydrothermal fluid types, unlike observed in Audétat et al. (2008) where brines precursor of the mineralization already showed enrichment of those metals. The two elements show a weak positive correlation with each other (Fig. 10h). In particular it is interesting to highlight the lack of a salinity-dependency of Sn, in contrast to what is observed in chlorine-normalized molar ratios of other typically chlorine-complexed elements such as Fe, Mn, Zn and Pb, in which high salinity fluids also possess the highest chlorine-normalized element ratios (Fig. 10d, e).

Arsenic displays a good overall correlation with salinity and is high in magmatic and hydrothermal samples, and lower in the transitional samples (Fig. 9). On the other hand, Sb increases slightly but progressively from late-magmatic to late-stage hydrothermal fluids (Fig. 9). Finally, Ba correlates positively with salinity but the concentration ranges are similar for all samples (typically between 1 and 100 ppm).

Magnesium and Al were part of the analyzed element suite, but were very prone to contamination of the fluid inclusion signals due to accidentally entrapped silicate phases or mineral inclusions such as muscovite within the host quartz. It was attempted to identify such contamination effects for each analyzed inclusion and subsequently remove these elements from the dataset of a given fluid inclusion. However, the few remaining concentration values for these elements still show relatively unsystematic and wide concentration ranges of 10 to 1000 ppm for Mg and 500 to 10,000 ppm for Al, indicating that not all contaminated signals were identified.

5. Discussion

5.1. Magmatic-hydrothermal processes recorded in fluid inclusions

The sample material studied records the protracted evolution of magmatic-hydrothermal systems in the Cornubian batholith from relatively early high-temperature to late low-temperature stages. In particular, specimens from granites, miarolitic cavities, pegmatites and barren quartz veins in G5 granite record the temporal compositional evolution related to early magmatic fractionation and to the dilution via externally derived fluids, while the remaining samples from greisens and polymetallic veins provide insights only about the latter stage. It is worth noting that each pluton of the system evolved at slightly different times, that the spatial distribution of the samples covers an area of 200 km and that they are associated with different granite types. Therefore, the observations discussed below cannot be considered a generalized temporal-compositional evolution of magmatic-hydrothermal systems of the entire Cornubian batholith, but rather represent insights into individual subsystems. Table 2 summarizes which processes were observed for each sample.

The complexity of interpreting fluid inclusion geochemical trends arises from the multitude of events that may influence the chemistry of the recorded fluid, the likelihood that such events repeat in a cyclic manner and superpose each other rather than forming a linear temporal

Table 2
Summary of the magmatic-hydrothermal processes observed for each sample, indicated with a cross, eventually bracketed if the observation is tentative.

Type	Sample	Magmatic fractionation	Phase separation	Dilution of ID fluid	Dilution of brine
Granite-related	21MD1		(x)		x
	21MD219		x		x
	21MD222	x		x	
	21MD100I	(x)		x	
	LELE	x	x	x	
Greisen	SCH1				x
Polymetallic	21MD65				x
	21MD10S				x
	21MD10B		(x)		x

sequence, and the fact that each element behaves differently across such events depending on partition coefficients, which are themselves strongly dependent on dynamically changing pressure and temperature conditions (Candela and Piccoli, 1995; Zajacz et al., 2008; Audétat et al., 2008; Audétat, 2019; Tattitch et al., 2021). However, a strong petrographic framework allows to ascribe chemical variations to individual events and reconstruct the likely events behind the various fluid types observed in the samples.

Based on the combination of petrography, microthermometry and geochemistry it is possible to distinguish two groups within the fluid type 1: "type 1a" is characterized by generally lower proportions of the vapor phase, overall lower salinity and homogenization temperature and a progressive decrease of trace elements with decreasing salinity; inclusions of "type 1b", on the other hand, have generally larger vapor bubbles, show petrographic evidence of being prior to the formation of brine inclusions and have higher salinity and homogenization temperature (referred hereafter as "intermediate density fluids", ID). This fundamental distinction allows to correctly interpret the fluid inclusion data in terms of time and significance of each fluid type, and was not taken into account in previous works in this area (cf. Drivenes et al., 2016). As described in the following sections, the difference in trends of type 1b compared to type 1a, is key in understanding the effect of individual magmatic-hydrothermal processes from each other.

Overall, no clear differences in time and chemistry were observed between brines of type 3 and 4, which are therefore discussed in this section as a single group. Notably, brine inclusions with more than one daughter crystals correlate with higher overall salinities. The effect of post-entrapment modifications on the geochemistry of the studied fluid inclusions is difficult to assess, as the mechanisms behind are not yet fully understood (Audétat, 2023) and we consider their effects to be minor for the following discussion. The FIAs for which such modifications have been inferred (see chapter 4.2.2, Fig. 7), in fact, do not deviate significantly in any Cl-normalized ratios from the FIAs in the rest of the sample (at lower salinities). In addition, the diffusion problem in quartz of Li and Cu in particular is acknowledged (Zajacz et al., 2009) and may have influenced the studied samples to some degree. However, given the clear compositional trends observed for these elements, similar to those seen for non-diffusive elements such as B, Fe and Zn, we nevertheless consider speculations on their behavior in the studied fluids to be valid.

5.1.1. Compositional evolution of early magmatic-hydrothermal fluids

The five samples discussed in this section include the fluid inclusion record in the magmatic quartz of the G3 granite from Dartmoor (21MD1) and in four G5 samples, including a granite (with inclusions hosted in both topaz and quartz, 21MD219) as well as a miarole (LELE) and a pegmatite (21MD100I), in which the earliest fluids were entrapped at temperatures above 420 °C at pressures above 1.5 kbar (see discussion below; isochores in Suppl. Fig. 1). Finally, the barren quartz vein sample in G5 granite (21MD222) is also included here: it is thought to have formed after a thermal collapse of the system, with the carapace of the G5 pluton being already solidified and cyclic overpressurization via continuous fluid release at depth leading to brittle failure and vein formation by ascending hot fluids. A similar scenario is plausible for the fluid inclusion record of the miarolitic cavity, which possibly contains fluids rising from the deeper crystallizing magma into the solidified rock overlying it.

5.1.2. Effects of fractional crystallization

It has been established that different pressure conditions affect the partitioning of trace elements between melt and fluid with progressive fractionation (Candela and Piccoli, 1995; Audétat et al., 2008; Audétat, 2019). Audétat (2019) showed that the concentrations of some elements (mainly chlorine-complexed cations such as Rb, Pb, Zn and Sn) show opposite behaviors, decreasing in fluids exsolved during progressive fractionation under "high pressure" conditions (above 1.5 kbar) and increasing during "low pressure" fractionation (below 1.2 kbar), whereas compositions of other elements (e.g. B, W) are unaffected by pressure conditions.

In the sample from the G5 miarolitic cavity (LELE) the fluid inclusion record displays at first glance an apparently simple trend of dilution of an intermediate density type 1b aqueous fluid, while a far more complicated picture emerges when considering the chemical evolution of the fluid. The homogenization temperatures systematically decrease from the core (starting at around 320 °C) to the rim of the crystal (around 150 °C) (Fig. 6) and salinities decrease from around 10 wt% $NaCl_{eq.}$ in the core to almost pure water in the rim (Fig. 9). The FIAs with the highest homogenization temperatures (320–290 °C), represent the earliest intermediate density fluids preserved in the sample (group w in Fig. 11). However, the subsequent decreases in salinity and homogenization temperatures in later FIAs, are characterized by increases in Cs, Rb, Li and B (group y in Fig. 11). This is consistent with the effect of magmatic fractionation under "high pressure" conditions, at ca. 1.5 kbar and above (Audétat, 2019). These observations are in agreement with previous pressure estimates for the Land's End pluton based on fluid inclusion work by Drivenes et al. (2016). One FIA (marked x in Fig. 11a, c, e, g) plot outside of this general fractionation trend and with regard to its microthermometric properties (Fig. 11i). Whether these rare fluids are genetically related to the early intermediate fluids of group w, or if they represent a separate short-lived fluid event cannot be unambiguously determined.

In the G5 pegmatite sample from the Tregonning-Godolphin stock (21MD100I), two main sets of fracture-hosted FIA orientations were recognized, as well as two distinct salinity groups (around 7 wt% and 1 wt% $NaCl_{eq.}$). In the higher salinity fluid (orange squares in Fig. 11), a slight increase in Rb and Cs with decreasing salinity, suggests that magmatic fractionation at pressure exceeding 1.5 kbar is plausible as well, although much less clear than sample LELE. In the syntaxial quartz vein in the G5 granite (sample 21MD222) salinity and homogenization temperatures in the fluids generally decrease from core to rim within individual crystals, from 11.2 wt% $NaCl_{eq}$ to 3.5 wt% $NaCl_{eq}$ and 390 °C to around 250 °C, respectively. The geochemical data reveals a fractionation trend of decreasing salinity with concomitant increases in Li, B, Rb and Cs in the intermediate density fluids, coherent again with continuous fluid exsolution during fractional crystallization at pressures above 1.5 kbar (Fig. 11).

The identification of fluid compositional trends consistent with fractional crystallization and progressive fluid exsolution in G5 granite samples is consistent with recent observations favoring magmatic formation of G5 granite as opposed to it being a product of metasomatic overprint of other granites (Manning and Hill, 1990; Stone, 1992; Simons et al., 2016).

5.1.3. Effects of fluid phase separation

Magmatic topaz and quartz are the principal hosts of fluid inclusions in the G5 granite sample (21MD219). The topaz grains are often overgrown by later quartz, which is also present as individual coarser crystals. Topaz-hosted FIAs are always aqueous type 1b fluids with salinities of ca. 18 wt% $NaCl_{eq.}$ and homogenization temperatures around 400 °C. Conversely, the quartz grains contain abundant type 3 brine inclusions (with salinities up to 43 wt% $NaCl_{eq.}$) in association with vapor-dominated type 2 L_5V inclusions, providing evidence of significant boiling during quartz formation, while earlier topaz formation occurred in the presence of intermediate density type 1b fluids. The quartz also hosts assemblages of aqueous, low salinity and low temperature type 1a fluids. Compositionally, the topaz-hosted intermediate density fluids (group "t" in Fig. 11) possess higher B and much higher Li contents than the brines (group "b", Fig. 11b, d). Assuming the brines to be the product of phase separation of the intermediate density topaz-hosted fluids, the compositional features are qualitatively consistent with experimental work on the partition coefficients of Li and B during boiling and phase separation, as both elements show a preference for the vapor phase (not

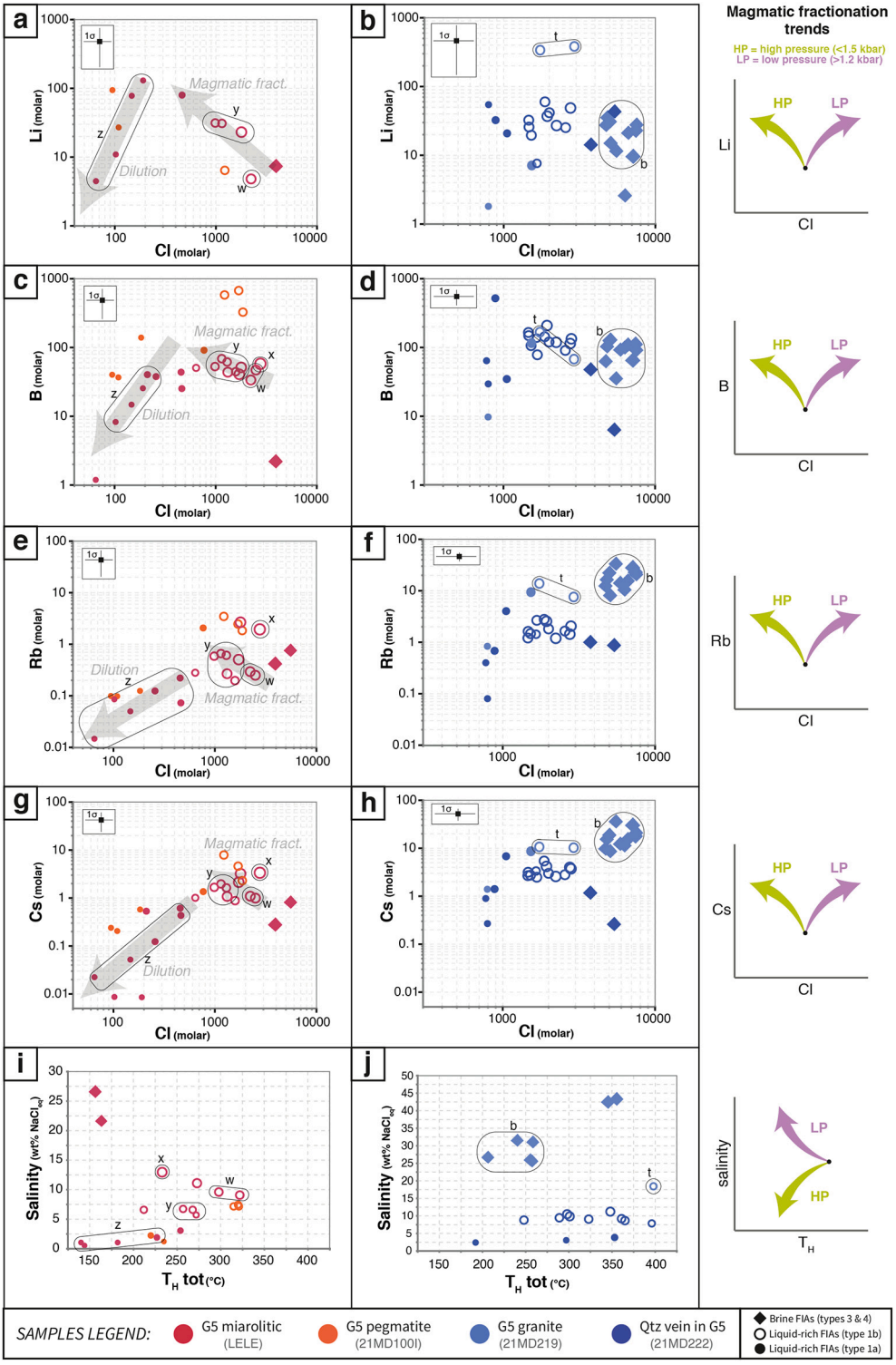

Fig. 11. Detailed geochemical diagrams showing Li, B, Rb and Cs concentrations versus Cl (a-h) and microthermometric data (salinity versus final homogenization temperature, i-j) showing the contrasting effects on geochemistry by magmatic fractionation and dilution (grey arrows). On the left sample data from the samples LELE and 21MD100I, while on the right half data from samples 21MD219 and 21MD222, all represented as FIA averages, with symbol size proportional to the salinity. On the rightmost part the magmatic fractionation trends that would occur at low pressure (LP, <1.2 kbar) and high pressure (HP, >1.5 kbar) for each set of diagrams, based on Audétat (2019). The distinction between liquid-dominated intermediate density fluids (open circles, type 1b) and diluted fluids (filled circles, type 1a) is highlighted. The abbreviations in the diagrams indicate selected FIAs with well-defined petrographic positions that allow to recognize individual magmatic-hydrothermal processes, see text for discussion. The median relative error for the plotted data is shown in each diagram.

analyzed) and should be depleted in brines compared to their precursor fluids (Heinrich et al., 1999; Foustoukos and Seyfried Jr, 2007). On the other hand, the affinity of Cs and Rb for the highly saline aqueous fluid during phase separation is confirmed by their similar or slightly higher concentrations in the brines compared to the intermediate density fluid (Fig. 11f, h). The brine inclusions form a compositional trend themselves, recording decreasing salinities and homogenization temperatures from 350 °C to 250 °C. Rubidium and Cs concentrations follow this trend, possibly indicating the onset of fluid dilution by external fluids in this stage.

In the miarolitic sample from G5 granite (LELE), few brine inclusion assemblages form rare secondary trails at the edge of the crystal and have homogenization temperatures of around 150 °C (indicated as red lines in Fig. 6, red diamond symbols in Fig. 11). The spatial association with more abundant vapor-dominated inclusions (compared to the core) suggest heterogeneous entrapment in a late low-pressure and low-temperature boiling system.

In the barren quartz vein sample (21MD222), type 3 brine inclusions (not forming clear FIAs and not analyzed by LA-ICP-MS) and type 2 vapor FIAs occur in spatial association, predominantly near the vein walls, while late low temperature boiling assemblages are found in the center of the vein and thus in the latest quartz crystals in the sample. This seems to indicate the occurrence of at least two boiling events, one contemporaneous with the crystallization of early quartz grains in the vein and one at a much later stage of vein formation. The late brine inclusions in the boiling FIAs at the center of the vein have low contents of Rb and particularly Cs compared to the intermediate density fluids in the same sample (Fig. 11f, h), and despite the impossibility of obtaining homogenization temperatures, their location at the center of vein and at rim of the latest quartz crystals indicate that they formed via very late boiling, in a similar fashion to the late boiling assemblages present in sample LELE (see above).

Finally, the G3 granite sample (21MD1), contains clear boiling assemblages with coexisting brine and vapor inclusions. As opposed to the previously described samples associated with G5 granites, there is no evidence for intermediate density type 1b fluids prior to the formation of brines. This may indicate that the fluid potentially exsolved directly in the two-phase state, reflecting shallow conditions during exsolution of

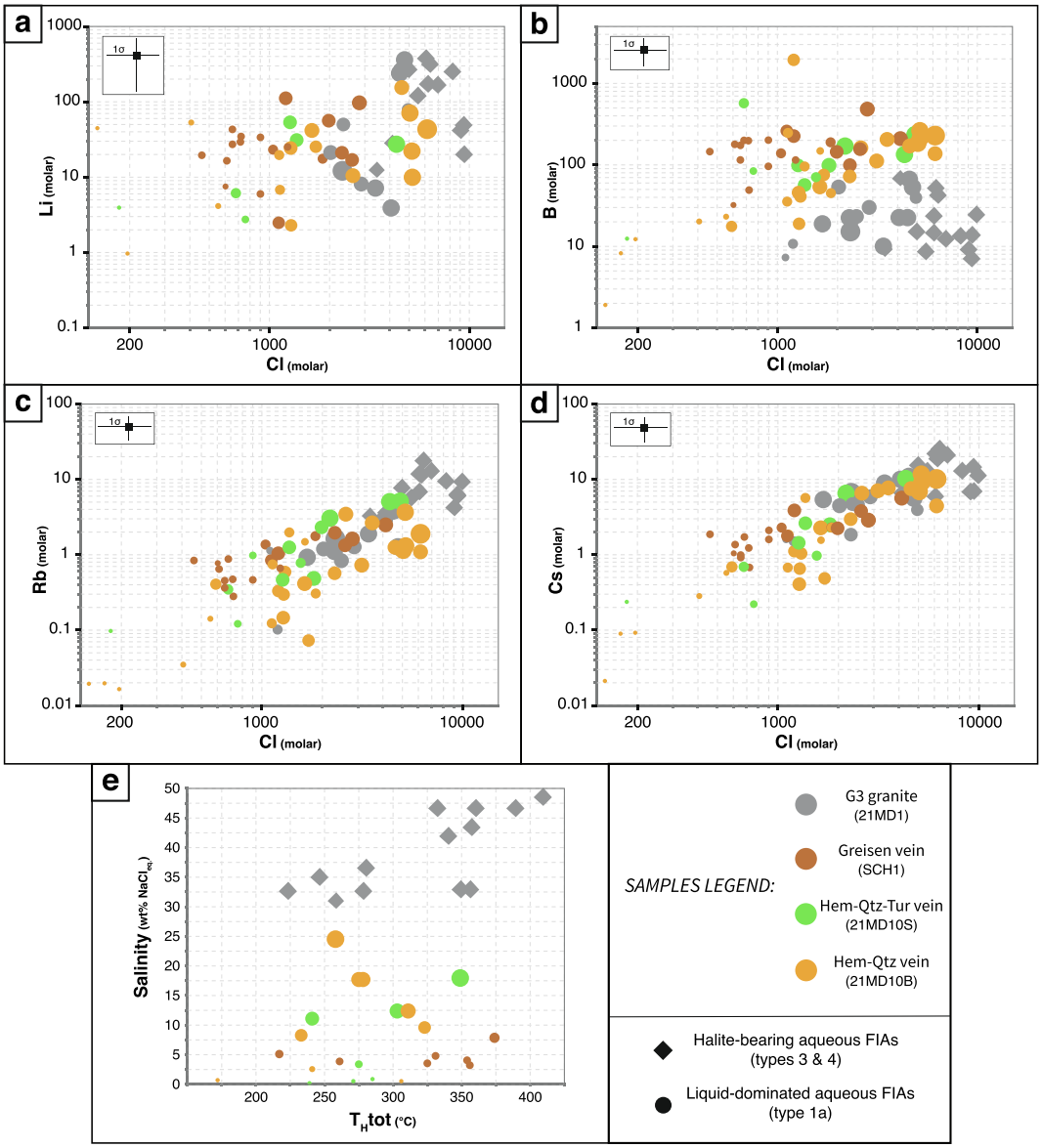

Fig. 12. Detailed geochemical diagrams with Li, B, Rb, Cs concentrations versus Cl and homogenization temperature versus salinity for the samples 21MD1, SCH1, 21MD10S and 21MD10B, where dilution is the only magmatic-hydrothermal process forming a clear trend. The median relative error for the plotted data is shown in each diagram.

magmatic fluids (Audétat, 2019). Such observation is corroborated by previous petrographic studies (Rankin and Alderton, 1983; Alderton and Harmon, 1991), which also pointed out the overall high abundance of high-salinity brines and vapor-rich aqueous inclusions as well as the low abundance of liquid-rich aqueous inclusions in granite samples from Dartmoor in comparison with granites from other plutons of the Cornubian batholith.

5.1.4. Evidence for dilution by external fluids

The G3 granite sample (21MD1) contains FIAs forming a continuous range of salinities from 48 wt% $NaCl_{eq.}$ brines to 5 wt% $NaCl_{eq.}$ aqueous fluids, accompanied by a parallel decrease in homogenization temperatures (Fig. 12). The trace element geochemistry is characterized by concomitant decreases of salinity and Cs, Rb and Li concentrations, whereas B is low already in the magmatic brines and remains constant (Fig. 12). There appears to be no high-pressure fractionation trend of decreasing salinity and increasing trace element concentrations, like those observed in the fluids in G5 granite systems (Fig. 11). The simple negative correlation of salinity and trace element concentrations also argues against a low-pressure magmatic fractionation trend (Audétat, 2019), as this should result in the lowest salinity fluids (i.e. the earliest fluids) possessing the highest homogenization temperatures, which was not observed (Fig. 12). We thus conclude that all fluids in this sample record various stages of dilution of a deeper-sourced brine formed by phase separation with external low-salinity fluids, leading to the formation of lower salinity and lower temperature type 1a fluids.

An alternative explanation for the observed concomitant decrease in both the metal content and salinity of the exsolving fluids could be the experimental and numerical modelling work by Tattitch et al. (2021). They show that for arc-related magmas, fluid salinities and Cu content systematically increase after the onset of fluid exsolution, but will eventually reach an inflection point after which fluids are also characterized by a progressively lower salinity and Cu concentration due to the fact that Cl eventually becomes depleted in the residual melt, which in turn lowers the solubility of chlorine-complexed elements (e.g. Cu) in the exsolving fluid. However, the former model does not apply to peraluminous systems such as the one of the Cornubian batholith and, importantly, we observe simultaneous decreases of salinity and concentration of all trace elements, including those not forming chlorine complexes (Figs. 11, 12). This would be inconsistent with existent experimental data, such as Audétat (2019), in a late stage fluid exsolution environment during fractional crystallization.

Despite smaller ranges of variation of salinity, similar dilution trends indicating a transformation of earlier fluids into type 1a fluids are also observed in the other samples containing early high-temperature type 1b and type 3–4 fluids discussed above. In Fig. 11, the onset of dilution is visualized by an inflection point and a sharp drop in salinity, trace element concentrations and homogenization temperatures, especially prominent in samples LELE (group z) and 21MD222.

5.1.5. Superposition of boiling and dilution processes

Interestingly, the B content in some of the lower salinity diluted type 1a FIAs is higher than that in the most highly evolved intermediate density type 1b fluids (Fig. 11c, d). Audétat et al. (2008) observed similar compositional trends with regard to Li, B and Cu in the Mole Granite (Australia) and interpreted it to reflect the partitioning behavior of B during boiling and phase separation. As B preferentially partitions into the buoyant low-density vapor phase, they proposed that these vapors ascended and condensed into the convecting meteoric fluid and strongly increased their B contents. Early boiling by cyclic depressurization could thus have caused a similar B enrichment in the convective cell surrounding the granite intrusions in the Cornubian batholith. The subsequent mixing of these pre-enriched fluids with the intermediate density fluids still present in deeper parts of the system could then very well explain the trends observed in Fig. 11d. An alternative hypothesis for the modifications in the chemistry of the circulating meteoric water would be fluid-rock interaction (Manning and Exley, 1984; Lecumberri-Sanchez et al., 2017), but since other trace elements do not show any further anomaly in the diluting fluids, the former model is preferred.

For Li, the fluids from the present study show contrasting trends, with high concentrations at the inflection point in samples from Tregonning-Godolphin (Fig. 11a), but not in samples from St. Austell (Fig. 11b), which may be due to local interaction with Li-rich minerals (in particular white micas) in the first case, or to the fact that Li does not always have a clear preference for the vapor phase (Foustoukos and Seyfried Jr, 2007). On the other hand, Cs and Rb decrease linearly during mixing with meteoric waters (Fig. 11e, g), reflecting the fact that these elements did not escape in the vapor phase but preferentially partitioned into the brines, in line with the expected behavior (Heinrich et al., 1999; Foustoukos and Seyfried Jr, 2007). Overall, the partitioning behavior of Li, B, Cs and Rb between vapor-rich fluids and brines is strongly consistent across all the samples presented.

5.1.6. Compositional trends in fluids related to greisen and polymetallic mineralization

All samples related to greisen (SCH1) or polymetallic mineralization show compositional evidence of progressive dilution of high-salinity magmatic-hydrothermal fluids by low-salinity external fluids, similar to the late-stage compositional trend observed for the previously discussed granite-related samples.

The fluorite-arsenopyrite-chalcopyrite vein sample (21MD65) represent the clearest petrographic evidence of progressive dilution of saline type 3 brines available in the sample set. In fact, the fluid inclusion record of this sample includes three distinct fluid types of high, intermediate and low salinity and all elements concentration (with the exception of As, which remains roughly constant) decrease linearly with salinity (Fig. 13), as do the homogenization temperatures. The progressive dilution of the magmatic fluid recorded in the fluid inclusions closely follows a hypothetic line of mixing with meteoric fluids (assuming an almost pure water end member, in different proportions, see percentages in Fig. 13). The only element that deviates from this trend is B, in favor of the hypothesis of post-boiling vapor buoyancy and mixing with convecting meteoric fluids described in the previous section.

In all the other samples dilution trends are also observed, with fluids showing a combined decrease of salinity, trace elements content and homogenization temperatures (Fig. 12). The fact that such trends are observed in various stages of the magmatic-hydrothermal systems suggests a protracted history of magmatic fluid dilution by low-salinity fluids. This is further exemplified in the late quartz-hematite polymetallic vein (21MD10B and 21MD10S) where a general trend of decreasing salinity is observed during multiple vein infill episodes interspersed with occasional inputs of high salinity fluids. The chemistry is not significantly different between the various fluid types, and all fluids show a progressive decrease of Li, B, Rb and Cs with decreasing salinity.

5.2. The origin of the diluting fluids in the Cornubian batholith

The dilution trend in all samples, and in particular in the polymetallic vein sample 21MD65 (Fig. 13) clearly shows that the fluid mixing with the magmatic one was approaching pure water composition (with the exception of B), clearly indicating a meteoric origin. Additionally, the presence of hematite coprecipitating with quartz in samples 21MD10B and 21MD10S, suggest oxidizing conditions of fluid, compatible with a meteoric source. In the other samples, similar observations can be made despite a more complex fluid inclusion record. This is in accordance with most of the studies previously done in this area (Simpson et al., 1979; Jackson et al., 1989). As discussed in section 5.1.1, the B anomaly is thought to be due to buoyant vapors condensing into the overlying circulating meteoric water before mixing again with the magmatic fluids.

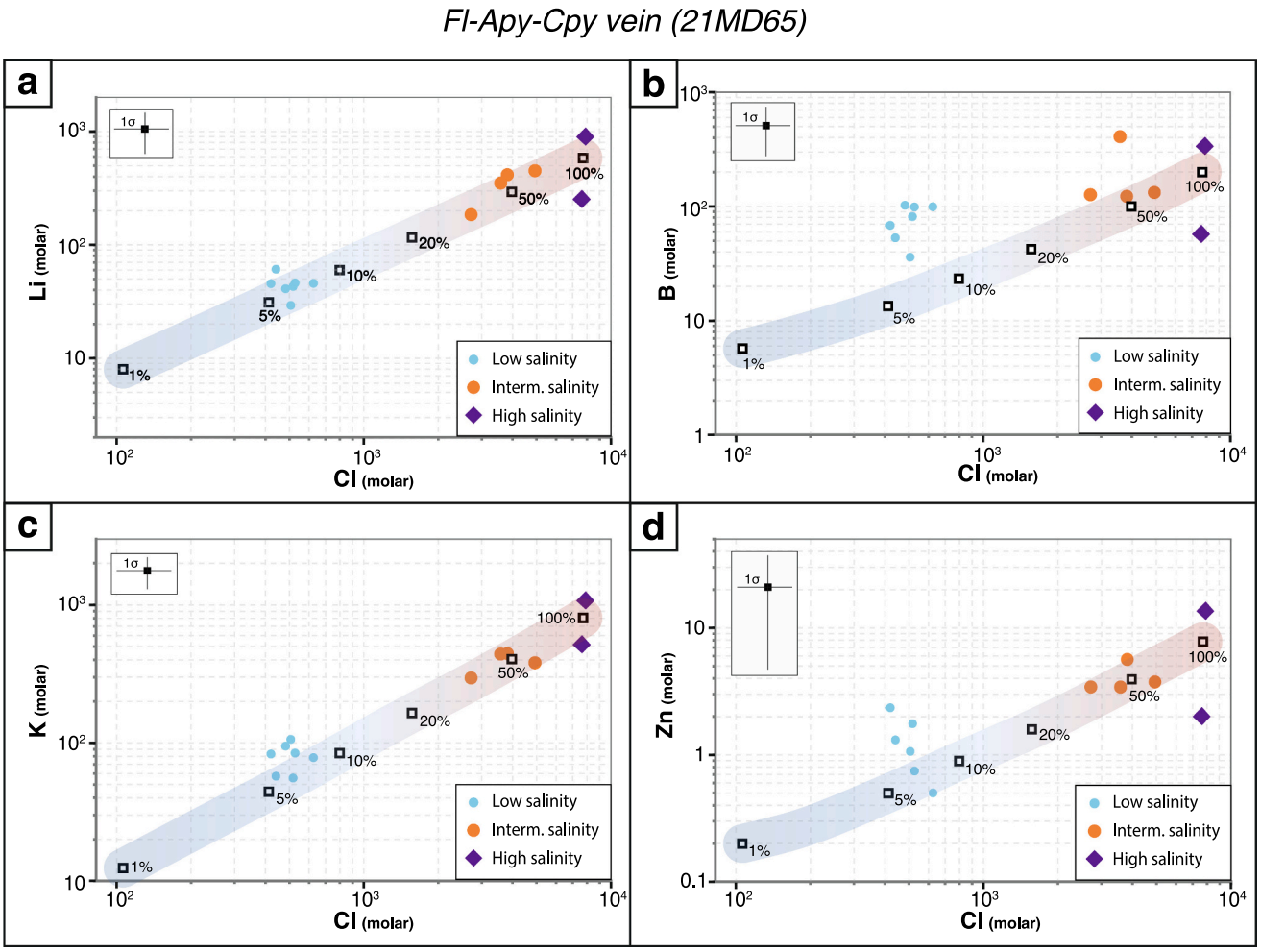

Fig. 13. Concentration of representative elements against Cl in sample 21MD65 (Fl-Apy-Cpy vein) showing linearly decreasing trends at decreasing salinity. The same trend as Li, K, Zn is observed also for Mn, Fe, Rb, Cs, Cu and Pb. The envelope represents the ideal concentration calculated by mixing the pure magmatic fluids (assumed as the average of the high salinity FIAs) with an estimated composition of meteoric waters. The squares indicate the different mixing ratio of magmatic fluid versus meteoric water. All elements except B follow the simulated concentrations envelope, with the lower salinity FIAs clustering at around 7% magmatic/meteoric ratio and the intermediate salinity FIAs around 40%. The error bars indicate the median relative error for each diagram. Abbreviations: Fl - fluorite; Apy - arsenopyrite; Cpy - chalcopyrite.

Formation waters rich in $CaCl_2$ are considered to play a major role during the formation of Triassic cross-course veins (Shepherd and Scrivener, 1987; Scrivener et al., 1994; Gleeson et al., 2000). These veins typically contain base metal sulfides, together with quartz, fluorite and barite as major gangue minerals. Such Ca enrichment was not identified in the hydrothermal samples studied here, and despite G3 granite fluids in Dartmoor having higher Ca/Na ratio than the other fluids, the age relationships and most importantly the homogenization temperatures are not compatible with mixing with $CaCl_2$ formation waters during magmatic-hydrothermal stages. It is therefore believed that such fluids did not play a significant role in the formation of greisen and polymetallic mineralization related to the Cornubian batholith.

5.3. Observations on Sn—W and base metals systematics

The positive correlation between salinity and chloride-complexing elements such as Fe, Mn, Pb and Zn in fluid inclusions from all samples is not surprising (Fig. 10). They all have the highest Cl-normalized values in the granite-related samples and progressively decrease upon dilution. Interestingly, the greisen fluids have very high concentrations of these elements, in particular Pb and Zn, whereas Sn, W and Cu are not as high in comparison to other samples. This anomaly probably indicates that the studied fluids represent spent fluids relative to the main Sn-W-(Cu) mineralization event, but are fertile for the formation of the more distal Pb-(Zn—Ag) veins.

The positive correlation between Sn and W is, on the other hand, more unexpected (Fig. 10h), as Sn typically complexes with Cl in hydrothermal fluids, whereas W does not and is rather carried as an oxyanion complex (Heinrich, 1990). Our data show that Sn and W do not correlate with salinity and therefore with Cl content (Fig. 10g). Sn/Cl and W/Cl are lowest in the high salinity FIAs, similarly to Li/Cl. However, as mentioned before, Li may be buffered by fluid-rock interaction and shows progressive decrease with higher degrees of dilution, in contrast to Sn and W that remain almost constant (Fig. 10g, h). In the case of Sn and W, no buffering minerals are evident and the processes behind their concentration and their relative correlation remain unclear.

W—Sn greisen veins are often spatially and temporally associated with G2 granites in the Cornubian batholith, and all the samples analyzed here (apart from the greisen vein sample itself, SCH1) are connected with G3 to G5 granites, whose exsolved fluids are likely successive in time and therefore their chemistry represents the post-greisen mineralization condition. On the other hand, Sn mineralization is known to occur also at a later stage, forming Sn-As-Cu polymetallic veins, and several cassiterite bearing veins are found to cut through G5 granites, especially in the St. Austell pluton. The samples from this study likely record fluid both prior and successive to this

mineralizing event, but there is not enough evidence to speculate on why the Sn content are overall low and constant in various types of fluids in different samples and the missing correlation between Sn and Cl remains enigmatic.

6. Conclusions

This work represents the first regional-scale geochemical fluid inclusion study on different granitic intrusion stages in the Cornubian batholith covering the entire evolution from magmatic to hydrothermal stages. The main findings are the following:

- Complex variations in fluid salinity are preserved in most studied samples, and are caused by a multitude of distinct processes, some of which were previously unrecognized. It is possible to distinguish the effects of magmatic fractionation, phase separation and fluid mixing (dilution with meteoric waters) on fluid chemistry through a combination of rigid petrography, microthermometry and in situ LA-ICP-MS microanalysis;
- Magmatic fractionation in samples related to G5 granite leads to decreasing salinity and increasing trace elements concentration in the exsolving intermediate density type 1b magmatic fluids, consistent with formation pressures exceeding 1.5 kbar. Later brine inclusions produced via phase separation record fluctuating pressure conditions (e.g. lithostatic to hydrostatic), and decreasing salinity and formation temperatures in late-stage type 1a inclusions indicate dilution by external fluids;
- The absence of intermediate density type 1b fluids prior to brine formation in the G3 granite of Dartmoor, consistent with previous studies, indicates fluid exsolution at shallow depths and low pressures (< 1 kbar);
- The samples related to greisen and polymetallic mineralization also show variable salinity that can be solely ascribed to dilution of type 1b and type 3–4 high-salinity magmatic fluids to form type 1a fluids;
- The diluting fluids compositionally approach pure water, suggesting a meteoric origin, except for their high B content which can be ascribed to its partitioning into the vapor phase and the subsequent escape into the convective fluid systems surrounding the intrusions.

This study illustrates the potential complexity of the fluid inclusion record in magmatic and hydrothermal rocks even within a single batholith, and that a variety of processes may lead to systematic salinity variations that could not be discerned without LA-ICP-MS fluid inclusion microanalysis. In turn, however, this complexity may also provide novel insight into formation and particularly pressure conditions for the formation of granitic Sn—W systems.

CRediT authorship contribution statement

Mauro Bongiovanni: Writing – review & editing, Writing – original draft, Investigation, Data curation, Conceptualization. **Tobias Fusswinkel:** Supervision, Project administration, Funding acquisition. **Michael A.W. Marks:** Supervision, Project administration, Funding acquisition.

Declaration of competing interest

The authors declare no competing interests for the production of the present manuscript.

Data availability

The data discussed in the article is made available as supplementary file (attached)

Acknowledgements

This project was supported by the Deutsche Forschungsgemeinschaft (DFG) as part of the Priority Program SPP-2238 “Dynamics of Ore Metals Enrichment”. The authors are grateful for the constructive suggestions by Dr. Chris Yeomans and an anonymous reviewer on this article, and to Marco Fiorentini for the editorial handling.

Appendix A. Supplementary data

Supplementary data to this article can be found online at https://doi.org/10.1016/j.chemgeo.2024.122119.

References

Alderton, D.H.M., 1993. Mineralization associated with the Cornubian granite batholith. In: Pattrick, R., Polya, D. (Eds.), Mineralization in the British Isles. Springer, pp. 270–354.
Alderton, D.H.M., Harmon, R.S., 1991. Fluid inclusion and stable isotope evidence for the origin of mineralizing fluids in south-West England. Mineral. Mag. 55, 605–611.
Alderton, D.H.M., Rankin, A.H., 1983. The character and evolution of hydrothermal fluids associated with the kaolinized St. Austell granite, SW England. J. Geol. Soc. Lond. 140, 297–309. https://doi.org/10.1144/gsjgs.140.2.0297.
Alderton, D.H.M., Rankin, A.H., Thompson, M., 1992. Fluid inclusion chemistry as a guide to tin mineralization in the Dartmoor granite, south-West England. J. Geochem. Explor. 46, 163–185. https://doi.org/10.1016/0375-6742(92)90078-M.
Allan, M.M., Yardley, B.W.D., Forbes, L.J., Shmulovich, K.I., Banks, D.A., Shepherd, T.J., 2005. Validation of LA-ICP-MS fluid inclusion analysis with synthetic fluid inclusions. Am. Mineral. 90, 1767–1775. https://doi.org/10.2138/am.2005.1822.
Audétat, A., 2019. The metal content of magmatic-hydrothermal fluids and its relationship to mineralization potential. Econ. Geol. 114, 1033–1056. https://doi.org/10.5382/econgeo.4673.
Audétat, A., 2023. A plea for more skepticism toward fluid inclusions: part II. Homogenization via halite dissolution in brine inclusions from magmatic-hydrothermal systems Is commonly the result of postentrapment modifications. Econ. Geol. 118, 43–55. https://doi.org/10.5382/econgeo.4974.
Audétat, A., Pettke, T., Heinrich, C.A., Bodnar, R.J., 2008. Special Paper: the Composition of Magmatic-Hydrothermal Fluids in Barren and Mineralized Intrusions. Econ. Geol. 103, 877–908. https://doi.org/10.2113/gsecongeo.103.5.877.
Bottrell, S.H., Yardley, B.W.D., 1988. The composition of a primary granite-derived ore fluid from S.W. England, determined by fluid inclusion analysis. Geochim. Cosmochim. Acta 52, 585–588. https://doi.org/10.1016/0016-7037(88)90114-7.
Breiter, K., Ďurišová, J., Hrstka, T., Korbelová, Z., 2018. The transition from granite to banded aplite-pegmatite sheet complexes: an example from Megiliggar Rocks, Tregonning topaz granite, Cornwall. Lithos 302–303, 370–388. https://doi.org/10.1016/j.lithos.2018.01.010.
Bristow, C.M., Exley, C.S., 1994. Historical and geological aspects of the China-clay industry of Southwest England. Trans. R. Geol. Soci. Cornwall 21, 247–314.
Campbell, A.R., Panter, K.S., 1990. Comparison of fluid inclusions in coexisting (cogenetic?) wolframite, cassiterite, and quartz from St. Michael’s Mount and Cligga Head, Cornwall, England. Geochim. Cosmochim. Acta 54, 673–681. https://doi.org/10.1016/0016-7037(90)90363-P.
Candela, P.A., Piccoli, P.M., 1995. Model ore-metal partitioning from melts into vapor and vapor/brine mixtures. In: Mineralogical Association of Canada Short Course Series, v. 23, pp. 101–127.
Chappell, B.W., Hine, R., 2006. The Cornubian Batholith: an example of magmatic fractionation on a crustal scale. Resour. Geol. 56, 203–244. https://doi.org/10.1111/j.1751-3928.2006.tb00281.x.
Chen, Y., Clark, A.H., Farrar, E., Wasteneys, H.A.H.P., Hodgson, M.J., Bromley, A.V., 1993. Diachronous and independent histories of plutonism and mineralization in the Cornubian Batholith, Southwest England. J. Geol. Soc. Lond. 150, 1183–1191. https://doi.org/10.1144/gsjgs.150.6.1183.
Chesley, J.T., Halliday, A.N., Snee, L.W., Mezger, K., Shepherd, T.J., Scrivener, R.C., 1993. Thermochronology of the Cornubian batholith in Southwest England: Implications for pluton emplacement and protracted hydrothermal mineralization. Geochim. Cosmochim. Acta 57, 1817–1835. https://doi.org/10.1016/0016-7037(93)90115-D.
Chi, G., Savard, M.M., 1997. Sources of basinal and Mississippi Valley-type mineralizing brines: mixing of evaporated seawater and halite-dissolution brine. Chem. Geol. 143, 121–125. https://doi.org/10.1016/S0009-2541(97)00096-X.
Clark, A.H., Chen, Y., Farrar, E., Wasteneys, H.A.H.P., Stimac, J.A., Hodgson, M.J., Willis-Richards, J., Bromley, A.V., 1993. The Cornubian Sn-Cu (-as, W) metallogenetic province: product of a 30 m.y. history of discrete and concomitant anatectic, intrusive and hydrothermal events. In: Proceedings of the Ussher Society, v. 8, pp. 112–116.
Cobbing, J., Clarke, M., 2006. Textural features of South-West England granites: a reinterpretation. Geosci. South West Engl. v. 11, 229–242.
Collins, J.H., Coon, J.M., 1914. On the topaz rock of St. Mewan Beacon, Cornwall, 15. Transactions of the Royal Geological Society of Cornwall, pp. 43–54.

Dangerfield, J., Hawkes, J.R., 1981. The Variscan Granites of south-West England: additional information. In: Proceedings of the Ussher Society, v. 5, pp. 116–120.
Dines, H.G., 1956. The Metalliferous Mining Region of South-West England: Memoir of the Geological Survey of Great Britain.
Dominy, S.C., Camm, G.S., Bussell, M.A., Scrivener, R.C., Halls, C., 1995. A review of tin stockwork mineralization in the south-West England orefield. Geosci. South West Engl. 8, 368–373.
Dominy, S.C., Camm, G.S., Bussell, M.A., 1996. Characteristics and development of carbona-style replacement tin mineralization in west Cornwall. In: Geoscience in South-West England, v. 9, pp. 97–104.
Driesner, T., Heinrich, C.A., 2007. The system H2O-NaCl. Part I: Correlation formulae for phase relations in temperature-pressure-composition space from 0 to 1000 °C, 0 to 5000 bar, and 0 to 1 XNaCl. Geochim. Cosmochim. Acta 71, 4880–4901. https://doi.org/10.1016/j.gca.2006.01.033.
Drivenes, K., Larsen, R.B., Müller, A., Sørensen, B.E., 2016. Crystallization and uplift path of late Variscan granites evidenced by quartz chemistry and fluid inclusions: example from the Land's End granite, SW England. Lithos 252, 57–75. https://doi.org/10.1016/j.lithos.2016.02.011.
Duchoslav, M., Marks, M.A.W., Drost, K., McCammon, C., Marschall, H.R., Wenzel, T., Markl, G., 2017. Changes in tourmaline composition during magmatic and hydrothermal processes leading to tin-ore deposition: the Cornubian Batholith, SW England. Ore Geol. Rev. 83, 215–234. https://doi.org/10.1016/j.oregeorev.2016.11.012.
Exley, C.S., Stone, M., 1964. The granitic rocks of South-West England. In: Hosking, K.F.G., Shrimpton, G.J. (Eds.), Present View of some Aspects of the Geology of Cornwall. Royal Geological Society of Cornwall, Penzance, pp. 131–184.
Foustoukos, D.I., Seyfried Jr., W.E., 2007. Trace element partitioning between vapor, brine and halite under extreme phase separation conditions. Geochim. Cosmochim. Acta 71, 2056–2071. https://doi.org/10.1016/j.gca.2007.01.024.
Fusswinkel, T., Wagner, T., Wälle, M., Wenzel, T., Heinrich, C.A., Markl, G., 2013. Fluid mixing forms basement-hosted Pb-Zn deposits: Insight from metal and halogen geochemistry of individual fluid inclusions. Geology 41, 679–682. https://doi.org/10.1130/G34092.1.
Fusswinkel, T., Giehl, C., Beermann, O., Fredriksson, J.R., Garbe-Schönberg, D., Scholten, L., Wagner, T., 2018. Combined LA-ICP-MS microanalysis of iodine, bromine and chlorine in fluid inclusions. J. Anal. At. Spectrom. 33, 768–783. https://doi.org/10.1039/c7ja00415j.
Gamble, B., Anderson, M., Griffiths, J.S., 2020. Hazards associated with mining and mineral exploitation in Cornwall and Devon, SW England. In: Giles, D.P., Griffiths, J.S. (Eds.), Geological Hazards in the UK: Their Occurrence, Monitoring and Mitigation – Engineering Group Working Party Report, v. 29. Geological Society, London, pp. 321–367. https://doi.org/10.1144/EGSP29.13.
Gleeson, S.A., Wilkinson, J.J., Shaw, H.F., Herrington, R.J., 2000. Post-magmatic hydrothermal circulation and the origin of base metal mineralization, Cornwall, UK. J. Geol. Soc. 157, 589–600. https://doi.org/10.1144/jgs.157.3.589.
Gleeson, S.A., Wilkinson, J.J., Stuart, F.M., Banks, D.A., 2001. The origin and evolution of base metal mineralising brines and hydrothermal fluids, South Cornwall, UK. Geochim. Cosmochim. Acta 65, 2067–2079. https://doi.org/10.1016/S0016-7037(01)00579-8.
Goldstein, R.H., Reynolds, T.J., 1994. Systematics of Fluid Inclusions in Diagenetic Minerals. SEPM Society for Sedimentary Geology.
Guillong, M., Meier, D.L., Allan, M.M., Heinrich, C.A., Yardley, B.W., 2008. SILLS : a MATLAB-based program for the reduction of laser ablation ICP-MS data of homogeneous materials and inclusions. In: Mineral Association of Canada Short Course, 40, pp. 328–333.
Hall, A., 1971. Greisenisation in the granite of Cligga Head, Cornwall. Proc. Geol. Assoc. 82, 209–230. https://doi.org/10.1016/S0016-7878(71)80003-2.
Harlaux, M., et al., 2021. The upper Oligocene San Rafael intrusive complex (Eastern Cordillera, Southeast Peru), host of the largest-known high-grade tin deposit. Lithos 400–401. https://doi.org/10.1016/j.lithos.2021.106409.
Heinrich, C.A., 1990. The chemistry of hydrothermal tin(−tungsten) ore deposition. Econ. Geol. 85, 457–481. https://doi.org/10.2113/gsecongeo.85.3.457.
Heinrich, C.A., Günther, D., Audétat, A., Ulrich, T., Frischknecht, R., 1999. Metal fractionation between magmatic brine and vapor, determined by microanalysis of fluid inclusions. Geology 27, 755–758. https://doi.org/10.1130/0091-7613(1999)027<0755:MFBMBA>2.3.CO;2.
Hosking, K.F.G., 1964. Permo-Carboniferous and later primary mineralisation of Cornwall and south- West Devon. In: Hosking, K.F.G., Shrimpton, G.J. (Eds.), Present View of some Aspects of the Geology of Cornwall. Royal Geological Society of Cornwall, Blackford, Truro, pp. 201–245.
Hosking, K.F.G., 1969. The nature of the primary tin ores of the South-West of England. In: Second Technical Conference on Tin (Bangkok). International Tin Council, London, pp. 1155–1244.
Hughes, S.P., 2018. The Tectonomagmatic Evolution of the Land's End Granite. University of Exeter.
Idoine, N.E., Raycraft, E.R., Price, F., Hobbs, S.F., Deady, E.A., Everett, P., Shaw, R.A., Evans, E.J., Mills, A.J., 2023. World Mineral Production: 2017–2021: Keyworth. Nottingham, British Geological Survey, p. 90.
Jackson, G.E.A., Power, G.M., 1995. Columnar, branching and curved feldspar growth in the St Michael's Mount granite, Cornwall. Proc. Ussher Society 8, 363–367.
Jackson, N.J., Halliday, A.N., Sheppard, S.M.F., Mitchell, J.G., 1982. Hydrothermal activity in the St just Mining District. In: Evans, A.M. (Ed.), Metallization Associated with Acid Magmatism. Wiley, pp. 137–179.
Jackson, N.J., Willis-Richards, J., Manning, D.A.C., Sams, M.S., 1989. Evolution of the Cornubian ore field, Southwest England: part II. Mineral deposits and ore-forming processes. Econ. Geol. 84, 1101–1133. https://doi.org/10.2113/gsecongeo.84.5.1101.
Korges, M., Weis, P., Lüders, V., Laurent, O., 2018. Depressurization and boiling of a single magmatic fluid as a mechanism for tin-tungsten deposit formation. Geology 46, 75–78. https://doi.org/10.1130/G39601.1.
LeBoutillier, N.G., 2002. The tectonics of Variscan magmatism and mineralisation in South West England. Univesity of Exeter. https://doi.org/10.13140/RG.2.2.33139.73764.
Lecumberri-Sanchez, P., Steele-MacInnis, M., Bodnar, R.J., 2015. Synthetic fluid inclusions XIX. Experimental determination of the vapor-saturated liquidus of the system H2O-NaCl-FeCl2. Geochim. Cosmochim. Acta 148, 34–49. https://doi.org/10.1016/j.gca.2014.08.015.
Lecumberri-Sanchez, P., Vieira, R., Heinrich, C.A., Pinto, F., Wälle, M., 2017. Fluid-rock interaction is decisive for the formation of tungsten deposits. Geology 45, 579–582. https://doi.org/10.1130/G38974.1.
Lehmann, B., 2020. Formation of tin ore deposits: A reassessment. Lithos 105756. https://doi.org/10.1016/j.lithos.2020.105756.
London, D., Manning, D.A.C., 1995. Chemical variation and significance of tourmaline from Southwest England. Econ. Geol. 90, 495–519. https://doi.org/10.2113/gsecongeo.90.3.495.
Manning, D.A.C., Exley, C.S., 1984. The origins of late-stage rocks in the St Austell granite - a re-interpretation. J. Geol. Soc. Lond. 141, 581–591.
Manning, D.A.C., Hill, P.I., 1990. The petrogenetic and metallogenetic significance of topaz granite from the Southwest England orefield. In: Special Paper of the Geological Society of America, 246, pp. 51–69. https://doi.org/10.1130/SPE246-p51.
Manning, D.A.C., Hill, P.I., Howe, J.H., 1996. Primary lithological variation in the kaolinized St. Austell Granite, Cornwall, England. J. Geol. Soc. 153, 827–838.
Moore, J.M.M., Jackson, N., 1977. Structure and mineralization in the Cligga granite stock, Cornwall. J. Geol. Soc. Lond. 133, 467–480. https://doi.org/10.1144/gsjgs.133.5.0467.
Mount, M., 1985. Geevor Mine: a review, *in* High heat production (HHP) granites, hydrothermal circulation and ore genesis. Conference 221–238.
Müller, A., Williamson, B.J., Smith, M., 2005. Origin of quartz cores in tourmaline from Roche Rock, SW England. Mineral. Mag. 69, 381–401. https://doi.org/10.1180/0026461056940258.
Müller, A., Seltmann, R., Halls, C., Siebel, W., Dulski, P., Jeffries, T., Spratt, J., Kronz, A., 2006. The magmatic evolution of the Land's End pluton, Cornwall, and associated pre-enrichment of metals. Ore Geol. Rev. 28, 329–367. https://doi.org/10.1016/j.oregeorev.2005.05.002.
Pettke, T., Oberli, F., Audétat, A., Guillong, M., Simon, A.C., Hanley, J.J., Klemm, L.M., 2012. Recent developments in element concentration and isotope ratio analysis of individual fluid inclusions by laser ablation single and multiple collector ICP-MS. Ore Geol. Rev. 44, 10–38. https://doi.org/10.1016/j.oregeorev.2011.11.001.
Polya, D.A., Foxford, K.A., Stuart, F., Boyce, A., Fallick, A.E., 2000. Evolution and paragenetic context of low δD hydrothermal fluids from the Panasqueira W-Sn deposit, Portugal: New evidence from microthermometric, stable isotope, noble gas and halogen analyses of primary fluid inclusions. Geochim. Cosmochim. Acta 64, 3357–3371. https://doi.org/10.1016/S0016-7037(00)00459-2.
Pownall, J.M., Waters, D.J., Searle, M.P., Shail, R.K., Robb, L.J., 2012. Shallow laccolithic emplacement of the Land's End and Tregonning granites, Cornwall, UK: Evidence from aureole field relations and P-T modeling of cordierite-anthophyllite hornfels. Geosphere 8, 1467–1504. https://doi.org/10.1130/GES00802.1.
Primmer, T.J., 1985. Discussion on the possible contribution of metamorphic water to the mineralizing fluid of south-West England: Preliminary stable isotope evidence. Proc. Ussher Society 6, 224–228.
Rankin, A.H., Alderton, D.H.M., 1983. Fluid inclusion petrography of SW England granites and its potential in mineral exploration. Mineral. Deposita 18, 335–347. https://doi.org/10.1007/BF00206483.
Rankin, A.H., Alderton, D.H.M., 1985. Fluids in granites from Southwest England, *in* High Heat Production (HHP) Granites. Hydrotherm. Circ. Gen. 287–299.
Scrivener, R.C., 1982. Tin and Related Mineralisation of the Dartmoor Granite. University of Exeter.
Scrivener, R.C., 2006. Cornubian granites and mineralization of SW England. In: Brenchley, P.J., Rawson, P.F. (Eds.), The Geology of England and Wales. The Geological Society, London, pp. 257–267.
Scrivener, R.C., Darbyshire, D.P.F., Shepherd, T.J., 1994. Timing and significance of crosscourse mineralization in SW England. J. Geol. Soc. Lond. 151, 587–590.
Scrivenor, J.B., 1903. The granite and greisen of Cligga Head (Western Cornwall): quarterly. J. Geol. Soc. Lond. 59, 142–159. https://doi.org/10.1144/GSL.JGS.1903.059.01-04.16.
Shail, R.K., Leveridge, B.E., 2009. The Rhenohercynian passive margin of SW England: Development, inversion and extensional reactivation. Compt. Rendus Geosci. 341, 140–155. https://doi.org/10.1016/j.crte.2008.11.002.
Shepherd, T.J., Scrivener, R.C., 1987. Role of basinal brines in the genesis of polymetallic vein deposits, Kit Hill - Gunnislake area, SW England. Proc. Ussher Society 6, 491–497.
Simons, B., Shail, R.K., Andersen, J.C.Ø., 2016. The petrogenesis of the early Permian Variscan granites of the Cornubian Batholith: lower plate post-collisional peraluminous magmatism in the Rhenohercynian Zone of SW England. Lithos 260, 76–94. https://doi.org/10.1016/j.lithos.2016.05.010.
Simons, B., Andersen, J.C.Ø., Shail, R.K., Jenner, F.E., 2017. Fractionation of Li, be, Ga, Nb, Ta, in, Sn, Sb, W and Bi in the peraluminous early Permian Variscan granites of the Cornubian Batholith: Precursor processes to magmatic-hydrothermal mineralisation. Lithos 278–281, 491–512. https://doi.org/10.1016/j.lithos.2017.02.007.

Simpson, P.R., Brown, G.C., Plant, J., Ostle, D., 1979. Uranium mineralization and granite magmatism in the British Isles. Philos. Trans. R Soc. Lond. 291, 385–412.
Smith, M., Banks, D.A., Yardley, B.W.D., Boyce, A., 1996. Fluid inclusion and stable isotope constraints on the genesis of the Cligga Head Sn-W deposit, S.W. England. Eur. J. Mineral. 8, 961–974. https://doi.org/10.1127/ejm/8/5/0961.
Steele-MacInnis, M., Bodnar, R.J., Naden, J., 2011. Numerical model to determine the composition of H2O-NaCl-CaCl2 fluid inclusions based on microthermometric and microanalytical data. Geochim. Cosmochim. Acta 75, 21–41.
Steele-MacInnis, M., Lecumberri-sanchez, P., Bodnar, R.J., 2012. HokieFlincs_H2O-NaCl: a Microsoft Excel spreadsheet for interpreting microthermometric data from fluid inclusions based on the PVTX properties of H2O-NaCl. Comput. Geosci. 49, 334–337.
Sterner, S.M., Hall, D.L., Bodnar, R.J., 1988. Synthetic fluid inclusions. V. Solubility relations in the system NaCl-KCl-H2O under vapor-saturated conditions. Geochim. Cosmochim. Acta 52, 989–1005. https://doi.org/10.1016/0016-7037(88)90254-2.
Stone, M., 1969. Nature and origin of banding in the granitic sheets Tremearne, Porthleven, Cornwall. Geol. Mag. 106, 142–158. https://doi.org/10.1017/S0016756800051955.
Stone, M., 1992. The Tregonning granite: petrogenesis of Li-mica granites in the Cornubian batholith. Mineral. Mag. 56, 141–155. https://doi.org/10.1180/minmag.1992.056.383.01.
Tapster, S., Shail, R., McAllister, H., Deady, E., McFarlane, J., 2017. Understanding the multi-episode formation of the world-class Hemerdon W–Sn deposit in the context of SW England granite evolution. Appl. Earth Sci. 126, 97–98. https://doi.org/10.1080/03717453.2017.1306298.
Tattitch, B., Chelle-Michou, C., Blundy, J., Loucks, R.R., 2021. Chemical feedbacks during magma degassing control chlorine partitioning and metal extraction in volcanic arcs. Nat. Commun. 12 https://doi.org/10.1038/s41467-021-21887-w.
Taylor, G.K., 2007. Pluton shapes in the Cornubian Batholith: New perspectives from gravity modelling. J. Geol. Soc. Lond. 164, 525–528. https://doi.org/10.1144/0016-76492006-104.
Torró, L., Harlaux, M., Castro-Morante, A., Vallance, J., Tavazzani, L., Bouvier, A.-S., Bovay, T., Chelle-Michou, C., Sempere, T., Carles Melgarejo, J., 2024. Tin mineralization in the Triassic Chacaltaya district (Cordillera real, Bolivia) traced by in situ c hemical and δ18O-δ11B compositions of tourmaline. Econ. Geol. 119, 471–500. https://doi.org/10.5382/econgeo.5051.
Wagner, T., Fusswinkel, T., Wälle, M., Heinrich, C.A., 2016. Microanalysis of fluid inclusions in crustal hydrothermal systems using laser ablation methods. Elements 12, 323–328. https://doi.org/10.2113/gselements.12.5.323.
Warr, L.N., Primmer, T.J., Robinson, D., 1991. Variscan very low-grade metamorphism in Southwest England: a diastathermal and thrust-related origin. J. Metamorph. Geol. 9, 751–764. https://doi.org/10.1111/j.1525-1314.1991.tb00563.x.
Wilkins, C., Jeffery, B., Speer, J., Dijkstra, A.H., McFarlane, J., 2017. Mineral assemblages and textures of granite-hosted veins in the Hemerdon W–Sn deposit: constraints from scanning electron microscope chemical X-ray mapping. Appl. Earth Sci. 126, 104–105. https://doi.org/10.1080/03717453.2017.1306306.
Wilkinson, J.J., 1990. The role of metamorphic fluids in the development of the Cornubian orefield: fluid inclusion evidence from South Cornwall. Mineral. Mag. 54, 219–230. https://doi.org/10.1180/minmag.1990.054.375.08.
Williamson, B.J., Stanley, C.J., Wilkinson, J.J., 1997. Implications from inclusions in topaz for greisenisation and mineralisation in the Hensbarrow topaz granite, Cornwall, England. Contrib. Mineral. Petrol. 127, 119–128. https://doi.org/10.1007/s004100050269.
Williamson, B.J., Spratt, J., Adams, J.T., Tindle, A.G., Stanley, C.J., 2000. Geochemical constraints from zoned hydrothermal tourmalines on fluid evolution and Sn mineralization: an example from fault breccias at Roche, SW England. J. Petrol. 41, 1439–1453. https://doi.org/10.1093/petrology/41.9.1439.
Willis-Richards, J., Jackson, N.J., 1989. Evolution of the Cornubian ore field, Southwest England: part I. Batholith Model. Ore Distrib. 84, 1078–1100.
Zajacz, Z., Halter, W.E., Pettke, T., Guillong, M., 2008. Determination of fluid/melt partition coefficients by LA-ICPMS analysis of co-existing fluid and silicate melt inclusions: Controls on element partitioning. Geochim. Cosmochim. Acta 72, 2169–2197. https://doi.org/10.1016/j.gca.2008.01.034.